Steady Wind-blown Cavities within Infalling Rotating Envelopes: Application to the Broad Velocity Component in Young Protostars

Lichen Liang, Doug Johnstone, Sylvie Cabrit, Lars E Kristensen

The Astrophysical Journal, 900:15 (24pp), 2020 September 1 https://doi.org/10.3847/1538-4357/aba830

Steady Wind-blown Cavities within Infalling Rotating Envelopes: Application to the Broad Velocity Component in Young Protostars

Lichen Liang[1], Doug Johnstone[2,3], Sylvie Cabrit[4], and Lars E. Kristensen[5]
[1] Institute for Computational Science, University of Zurich, Winterthurerstrasse 190, Zurich, Switzerland
[2] National Research Council Canada, Herzberg Astronomy & Astrophysics, 5071 West Saanich Road, Victoria, BC, V9E 2E7, Canada
doug.johnstone@nrc-cnrc.gc.ca
[3] Department of Physics & Astronomy, University of Victoria, Victoria, BC, V8P 5C2, Canada
[4] Observatoire de Paris, PSL University, Sorbonne Université, CNRS, LERMA, 61 Av. de l'Observatoire, F-75014, Paris, France
[5] Niels Bohr Institute & Centre for Star and Planet Formation, University of Copenhagen, Øster Voldgade 5–7, DK-1350 Copenhagen K, Denmark
Received 2020 June 4; revised 2020 July 18; accepted 2020 July 20; published 2020 August 27

Abstract

Wind-driven outflows are observed around a broad range of accreting objects throughout the universe, ranging from forming low-mass stars to supermassive black holes. We study the interaction between a central isotropic wind and an infalling, rotating envelope, which determines the steady-state cavity shape formed at their interface under the assumption of weak mixing. The shape of the resulting wind-blown cavity is elongated and self-similar, with a physical size determined by the ratio between wind ram pressure and envelope thermal pressure. We compute the growth of a warm turbulent mixing layer between the shocked wind and the deflected envelope, and calculate the resultant broad-line profile, under the assumption of a linear (Couette-type) velocity profile across the layer. We then test our model against the warm broad velocity component observed in CO $J = 16$–15 by Herschel/HIFI in the protostar Serpens-Main SMM1. Given independent observational constraints on the temperature and density of the dust envelope around SMM1, we find an excellent match to all its observed properties (line profile, momentum, temperature) and to the SMM1 outflow cavity width for a physically reasonable set of parameters: a ratio of wind to infall mass flux of ≃4%, a wind speed of $v_w \simeq 30$ km s^{-1}, an interstellar abundance of CO and H_2, and a turbulent entrainment efficiency consistent with laboratory experiments. The inferred ratio of ejection to disk accretion rate, ≃6%–20%, is in agreement with current disk wind theories. Thus, the model provides a new framework to reconcile the modest outflow cavity widths in protostars with large observed flow velocities. Being self-similar, it is applicable over a broader range of astrophysical contexts as well.

Unified Astronomy Thesaurus concepts: Stellar jets (1607); Stellar winds (1636); Protostars (1302); Accretion (14); Stellar-interstellar interactions (1576); Astrochemistry (75)

1. Introduction

Massive outflows are observed everywhere in the universe, ranging from individual forming stars through galactic-scale events. When supersonic stellar or galactic winds interact with the surrounding medium, be it the molecular envelope around forming stars or the intergalactic gas, they are observed to impart momentum and energy, and entrain a slower-moving massive outflow. The actual entrainment mechanism and efficiency, however, remain poorly understood and highly debated, both because of a lack of strong observational constraints as well as a relative paucity of theoretical predictions against which to test observations.

A specific example of entrainment takes place when an accreting protostar launches a highly collimated jet, possibly surrounded by a wider-angle disk wind, carving out a large and slow massive outflow cavity into the parent cloud (Frank et al. 2014). When the Herschel Space Observatory (Pilbratt et al. 2010) started observing protostars in H_2O and high-J CO rotational transitions, it quickly became clear that the dominant source of the emission was from molecular outflows (e.g., van Dishoeck et al. 2011; Kristensen et al. 2012, 2017). It also became clear that these emission lines highlight a different outflow component from the low-J CO transitions observed from the ground, such as $J = 2$–1 and 3–2 (e.g., Yildiz et al. 2013). This Herschel-bright outflow component has both a significantly higher temperature ≃200–500 K and a larger line width at half maximum (FWHM) $\geqslant$ 30 km s^{-1} compared to low-J CO line profiles, where it only appears as a faint pedestal in very deep integrations (Margulis & Snell 1989). Accordingly, it was labeled the "broad" outflow component (Kristensen et al. 2012, 2017; Mottram et al. 2014, 2017).

The physical origin of the "broad" warm outflow component, and its relation to both the slower cold outflow, seen in low-J emission, and the faster protostellar jet or wind, is not clear. Two hypotheses have been put forward: either this broad component arises within a warm and dusty disk wind (Panoglou et al. 2012; Yvart et al. 2016) or it arises where ambient material is currently being entrained into the outflow by the protostellar wind, for example, through nondissociative shock waves (Kristensen et al. 2012, 2017; Mottram et al. 2014, 2017). While detailed, dynamical, and thermochemical predictions exist for the disk wind models, which reproduce the observed H_2O emission (Yvart et al. 2016), only limited model predictions exist in the literature for the entrainment scenario, and it thus remains a hypothesis. The underlying physical issue is not a problem reserved for protostellar outflows, but it remains an uncertainty for outflows in general.

The first type of entrainment scenario proposes that outflows are entrained by large jet bow shocks. These models predict substantial warm molecular material at intermediate velocities

(e.g., Raga & Cabrit 1993; Downes & Cabirt 2003), but the resulting outflow cavities have been deemed too elongated compared to observations (Ostricker et al. 2001). To avoid this potential issue, the second type of entrainment scenario proposes that entrainment is dominated instead by a wide-angle wind. A particularly popular version of this "wind-driven" scenario assumes instantaneous full mixing between the shocked isotropic wind and the shocked envelope material. Due to the complete mixing, the cavity retains a primarily radial outflow motion with a roughly constant expansion speed over time (Li & Shu 1996; Lee et al. 2000), except very close to the disk midplane where the cavity remains trapped near the outer disk radius (Wilkin & Stahler 2003; Mendoza et al. 2004; López-Vázquez et al. 2019). Such a radially expanding wind-blown cavity, however, grows too quickly: with expansion speeds $\geqslant$10 km s^{-1} similar to those observed in the broad component, it exceeds the typical radius of $\leqslant$3000 au of protostellar outflow cavities (see, e.g., Lee et al. 2015; Gueth et al. 1998, for HH212 and L1157, respectively) in only a few 1000 yr (Shang et al. 2006; López-Vázquez et al. 2019). This timescale is much shorter than the typical age accepted for Class 0 outflow sources (10^4–10^5 yr; e.g., Kristensen & Dunham 2018, and references therein).

In order to circumvent this "age" problem, in this paper we consider wind-driven cavities with partial mixing, instead of full mixing, and explore *stationary solutions* for the cavity shape, formed as the fast stellar wind is obliquely deflected by the envelope and forced to flow along the cavity wall instead of radially outward. Indeed, numerical simulations of a spherical wind propagating into a rotating and infalling slab show that when mixing is inefficient, the cavity "flanks" quickly converge to a quasi-steady shape (Delamarter et al. 2000). A modest outflow cavity width can then be maintained over the whole duration of the Class 0 phase. Such a configuration is also prone to the development of a turbulent mixing layer at the contact discontinuity between the shocked wind and the shocked envelope gas, as they slide past one other (Raga et al. 1995). In this paper, we will therefore follow a deliberate path to testing whether such a mixing layer might explain the broad spectral component observed around protostars by Herschel/HIFI and, at the same time, the observed cavity sizes.

Steady wind cavity solutions were first computed by Brral & Cantó (1981) for an isotropic wind expanding into a thick isothermal self-gravitating toroid. Smith (1986) showed that similarly elongated "flame-like" cavities could also be obtained for isotropic envelopes with a purely radial pressure profile $p(r) \propto r^{-n}$, provided that $n < 2$ and the wind is obliquely deflected at its closest point of impact (e.g., by a small-scale thin disk). Both of these early calculations show that the addition of a dense, disk-like component along the horizontal axis can provide the required equatorial pinch to create steady, elongated outflow shapes similar to those observed around protostars. Similar physical conditions are expected for galactic-scale outflows (see, e.g., Aalto et al. 2016). In this paper, we proceed one step further than these previous investigations by computing stationary solutions in a more realistic density and velocity distribution for the envelope, namely, the more sophisticated Ulrich (1976) infalling and rotating solution. Despite an identical ambient density distribution, our cavity morphologies will strongly differ from the calculations of Wilkin & Stahler (2003), Mendoza et al. (2004), and López-Vázquez et al. (2019) in that we assume weak mixing, instead of full mixing, between the shocked wind and the shocked envelope, and we include the effect of thermal pressure in the envelope. These two ingredients allow the existence of stable stationary solutions on large scales, with pointed shapes at the pole.

In Section 2 we determine the stationary cavity shape formed by a wide-angle wind deflected by an infalling and rotating protostellar envelope. In Section 3 we consider the deflected wind material flowing along the cavity boundary and the turbulent entrainment of envelope material within a mixing layer. We then, in Section 4, compute the angular momentum and synthetic line profiles associated with material within the mixing layer. Next, we quantitatively compare the model results against observations from Herschel of the broad CO component in the protostar Serpens-Main SMM1 (Section 5). Finally, in Section 6, we conclude with a recap of the implications of these results.

2. Determination of the Cavity Shape

In this section, we produced by an isothermal Ulrich (1976) infalling and rotating envelope model interacting with an isotropic wind. We determine the fundamental nondimensional parameters and characteristic values and perform a stationary solution analysis in order to determine the range of cavity shapes produced. The shape of the thin shell formed by this interaction is determined by the (ram plus thermal) pressure balance between the wind and the envelope along with a "centrifugal term" due to the upward curving motion of the shocked wind layer.

The analyses in this section, as well as in Section 3 and Section 4, are presented in dimensionless form in order to focus on the underlying self-similarity of the shape and the scaling relations underpinning the solutions, which have general applicability for all manner of outflows. In Section 5, we adopt appropriate physical values in order to quantitatively determine the agreement between the model and observations, in the specific case of a warm CO outflow of a nearby protostar.

2.1. Infalling and Rotating Envelope Model

The Ulrich (1976) infalling envelope model generalizes from the case of an isothermal cloud by combining the spherical infall of envelope material under the force of gravity due to the mass of the central object $M_\star$ (Bondi 1952) together with a treatment of the centrifugal deflection of the flow due to initial solid-body rotation. Thus, in the outer envelope, before angular momentum becomes dominant, the density structure is almost spherical with $\rho(r) \propto r^{-3/2}$. At smaller radii, where centrifugal forces dominate, the flow streamlines are deflected toward the midplane, creating a disk-like structure inside the fiducial radius

$$r_{\rm d} = \frac{\Gamma_\infty^2}{G\,M_\star}. \quad (1)$$

Here, Γ_∞ is the specific angular momentum in the equatorial plane. Assuming a ballistic solution for the infalling material, the entire envelope solution can be described by a handful of parameters: the mass of the protostar $M_\star$, the size of the disk $r_{\rm d}$, and the mass infall rate $\dot{M}_{\rm inf}$.

Following Ulrich (1976), we therefore find for the density in the envelope

$$\rho_{\rm inf}(r,\,\theta) = \frac{\dot{M}_{\rm inf}}{8\pi (GM_\star r^3)^{1/2}}\left(1+\frac{\sin\theta}{\sin\theta_0}\right)^{-1/2} \times \left(\frac{\sin\theta}{2\sin\theta_0}+\frac{r_{\rm d}\sin^2\theta_0}{r}\right)^{-1}, \quad (2)$$

where r is the spherical radius, θ is measured from the disk plane, and the subscript "0" denotes the initial value at a very large distance from the origin. At any location $(r,\,\theta)$ in the infalling envelope, the initial angular origin of the streamline, θ_0, can be obtained by solving

$$r = \frac{r_{\rm d}\sin\theta_0\cos^2\theta_0}{\sin\theta_0-\sin\theta}. \quad (3)$$

Finally, the three components of the velocity of the infalling material at the position $(r,\,\theta)$ are given by

$$v_{\rm inf,r} = -\left(\frac{GM_\star}{r}\right)^{1/2}\left(1+\frac{\sin\theta}{\sin\theta_0}\right)^{1/2}, \quad (4)$$

$$v_{{\rm inf},\theta} = -\left(\frac{GM_\star}{r}\right)^{1/2}(\sin\theta_0-\sin\theta)\left(\frac{\sin\theta_0+\sin\theta}{\sin\theta_0\cos^2\theta}\right)^{1/2}, \quad (5)$$

and

$$v_{{\rm inf},\phi} = -\left(\frac{GM_\star}{r}\right)^{1/2}\frac{\cos\theta_0}{\cos\theta}\left(1-\frac{\sin\theta}{\sin\theta_0}\right)^{1/2}. \quad (6)$$

Note that we have corrected the typographical error in Equation (8) of Ulrich (1976) as noted by Tobin et al. (2012).

2.2. Wide-angle Wind

In this paper, we assume a spherical isotropic wide-angle wind of constant speed $v_{\rm w}$ and mass-loss rate $\dot{M}_{\rm w}$, with the density profile

$$\rho_{\rm w} = \frac{\dot{M}_{\rm w}}{4\pi v_{\rm w} r^2}. \quad (7)$$

This approach enables a useful comparison with previous work (Brral & Cantó 1981; Smith 1986; Wilkin & Stahler 2003; Mendoza et al. 2004; López-Vázquez et al. 2019) and applicability to a wide range of astrophysical contexts.

For example, while observations of young stars and Class 0 protostars show a strong and fast jet-like component along the axis, surrounded by a (seemingly) mostly empty lower-velocity outflow cavity, several MHD models predict that the jet may only be an "optical illusion" and may represent only the central densest core of a wider-angle wind, launched either from the inner disk edge ("X-wind" model; Shang et al. 1998) or from a larger portion of the disk surface ("D-wind" model; Cabrit et al. 1999).

Thus, in the context of protostellar outflows, the isotropic wide-angle wind provides an acceptable approximation to the X-wind in equatorial regions, where the interaction is the most critical to defining the overall cavity shape (see below). We note that the addition of a strongly directed jet-like wind enhances breakout along the outflow axis and will thus modify the cavity shape in the polar regions. Comparison with observations should thus focus on regions close to the flow base, at wide angles to the flow axis.

2.3. Determining Fundamental Nondimensional Parameters and Characteristic Values

The trapping, breakout, and early evolution of the cavity formed by an isotropic wind colliding against an Ulrich (1976) infalling envelope were first calculated under the full mixing hypothesis, including stellar gravity and various degrees of wind collimation (Wilkin & Stahler 2003), and envelope rotation (López-Vázquez et al. 2019). Full mixing requires that the shell expansion is almost radial, hence the effect of thermal pressure in the envelope was ignored compared to the infall ram pressure in the frame of the expanding shell. A simplified study of the asymptotic shell expansion based on simple ram pressure balance was conducted by Mendoza et al. (2004). The authors show that it depends only on a single free parameter, namely the ratio of wind ram pressure to the fiducial infall ram pressure at $r_{\rm d}$,

$$\lambda \equiv \frac{v_{\rm w}\,\dot{M}_{\rm w}}{v_{\rm d}\,\dot{M}_{\rm inf}}, \quad (8)$$

where

$$v_{\rm d} = (GM_\star/r_{\rm d})^{1/2} \quad (9)$$

is the Keplerian velocity at $r_{\rm d}$.

Trapped solutions with sizes less than $r_{\rm d}$ were found for $\lambda \lesssim 1/2$ (see Figures 5 and 8 from Mendoza et al. 2004). For values of $\lambda > 1/2$, the cavity solutions were found to break out and expand forever, remaining pinched only along the disk midplane near $r_{\rm d}$. Similar results were found by Wilkin & Stahler (2003) and López-Vázquez et al. (2019), with an additional breakout criterion on $v_{\rm w}/v_{\rm d}$ for the polar cap to escape stellar gravity. For the X-wind and D-wind models currently favored in protostars, the denser and faster jet-like components along the axis will greatly facilitate breakout along the pole compared with the requirements for an isotropic wind (see discussion in Wilkin & Stahler 2003). Therefore, here we will assume that initial breakout has occurred and not consider this velocity constraint in our models.

In the present investigation, we are interested in finding steady asymptotic solutions to these breakout scenarios. For this, we assume instead that at most weak mixing occurs between the shocked wind and the shocked envelope material. Under this assumption, these two shocked and deflected layers will flow past each other, with an intermediate thin mixing layer developing along the contact discontinuity between them.

A further difference between our models and those of Wilkin & Stahler (2003), Mendoza et al. (2004), and López-Vázquez et al. (2019) is that we take into account the role of thermal pressure in the envelope in confining the shell. This is the crucial element allowing a steady configuration to be reached on large scales, instead of infinite expansion. Given that the density distribution in the envelope retains a modified, $r^{-3/2}$, power law, we anticipate that the resulting steady cavities will appear similar to the Smith (1986) elongated outflow cavities.

We thus introduce a characteristic scale length, $r_{\rm s}$, as the location where the ram pressure in the wind, $\rho_{\rm w}v_{\rm w}^2$, is balanced by the thermal pressure in the equivalent spherically symmetric infalling envelope, $\rho_{\rm inf}c_{\rm s}^2$. Solving this equality yields

$$r_{\rm s} = \left(\frac{v_{\rm w}\,\dot{M}_{\rm w}}{\dot{M}_{\rm inf}}\right)^2\frac{2GM_\star}{c_{\rm s}^4} = \frac{2GM_\star v_0^2}{c_{\rm s}^4}, \quad (10)$$

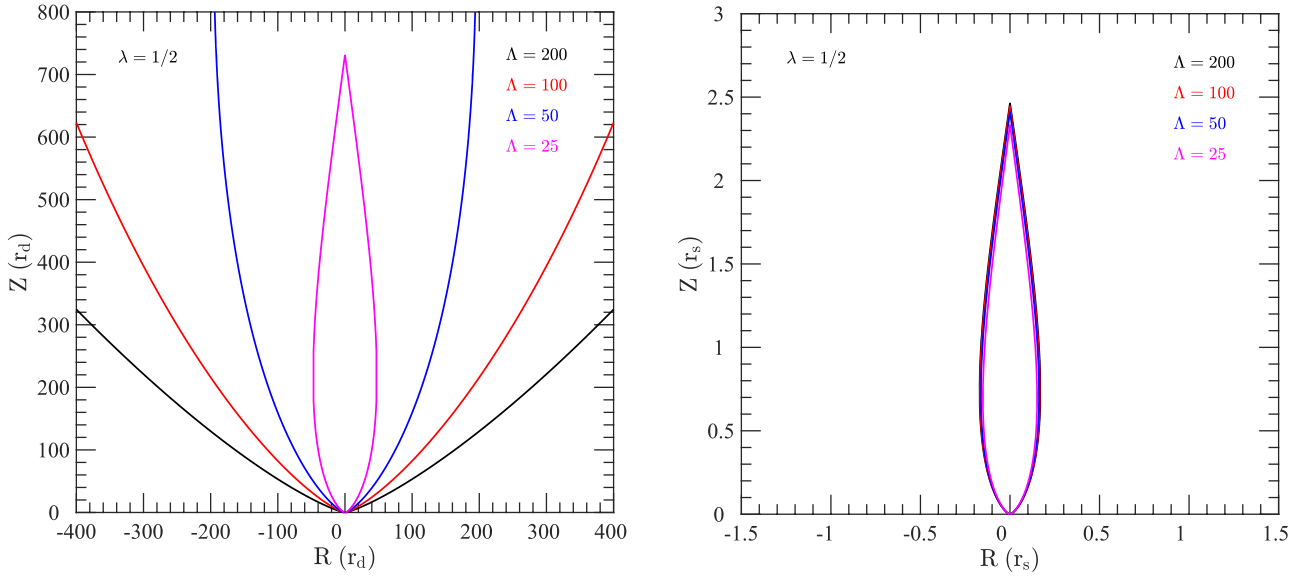

Figure 1. Cavity shapes for an isotropic wind colliding with an Ulrich (1976) infalling envelope for a range of Λ values (in all cases $\lambda = 1/2$). The left panel plots the results in units of r_d. The right panel reveals the self-similarity of the solutions under the transformation to $r_s = 0.5\,\Lambda^2\,r_d \equiv 2\,GM_\star(v_w\dot{M}_w/\dot{M}_{inf})^2\,c_s^{-4}$, which determines the physical scale of the cavity.

where we define the useful characteristic velocity v_0, fixed by the source ejection versus accretion physics, as

$$v_0 \equiv v_w\left(\frac{\dot{M}_w}{\dot{M}_{inf}}\right) = c_s^2\sqrt{\frac{r_s}{2GM_\star}}. \quad (11)$$

Another region where thermal pressure will dominate the infall ram pressure is near the equator, where the cavity is strongly pinched at $r \simeq r_d$ (see López-Vázquez et al. 2019) such that infall motions become almost parallel to the cavity walls. This introduces a second fundamental nondimensional parameter in our model, Λ, which is proportional to the ratio of wind ram pressure to envelope thermal pressure at r_d:

$$\Lambda \equiv \sqrt{\frac{2r_s}{r_d}}, \\ = 2\lambda\mathcal{M}_d^2, \quad (12)$$

where

$$\mathcal{M}_d = \frac{v_d}{c_s} \quad (13)$$

is the Mach number of the infall velocity at r_d. We show in the next section that Λ only affects the cavity shape very close to the disk midplane, where it determines the initial footpoint and opening angle.

While the disk centrifugal radius r_d provides an appropriate scaling for the geometry at the flow base, we expect r_s to provide an appropriate scaling for the geometry at large distances from the disk, where the cavity is confined by the thermal pressure in the envelope, rather than by the infall ram pressure.

Finally, we note that while trapped solutions confined by gravity on small scales, $\leqslant r_d$, were shown to be unstable, our steady shells on large scales, $\gg r_d$, are confined by thermal and ram envelope pressure and thus expected to be stable (see discussion in Wilkin & Stahler 2003). Moreover, our assumption of weak (instead of full) mixing allows a nonradial escape route for the bulk of the material reaching the shell by either moving upward (wind) or downward (envelope). Such situations are much more stable against wind or infall variations than the full mixing case. This is supported by the robustness of the shell shape with respect to changes in initial or global parameters.

2.4. Calculating the Cavity Shape

To determine the location of the static boundary where the wind interacts obliquely with the infalling envelope, we follow the formalism of Matsuyama et al. (2009; their Equations (2)–(5), which are derived in the appendix to that paper), which keeps track of both the mass and momentum flux deposited along the boundary by the shocked wind on the inner side and by the infalling material on the outer side.

The starting condition that $\partial r/\partial\theta = 0$ at the pole, used to compute cavity shapes with full mixing (e.g., López-Vázquez et al. 2019), is no longer a requirement in the case of weak mixing, where flame-like shapes are allowed. Instead, we integrate from the disk midplane up, following Smith (1986). A starting location in the disk, which also explicitly sets the angle of incidence, is thus required in order to solve these equations. As noted above, López-Vázquez et al. (2019) find that breakout solutions lead to a strong pinch on the disk plane near $r \lesssim r_d$. We have performed a detailed analysis of the possible angles of incidence allowed at the midplane as a function of $r/r_d < 1$ for all combinations of λ and Λ (see Appendix A). We find that when the cavity is forced to meet the midplane at $r/r_d \ll 1$, the required angle of incidence at the midplane is such that the infalling streamlines approach the cavity wall from inside the cavity—an unphysical solution. As the midplane crossing approaches r_d, however, there always exists a location where the angle of incidence of the cavity with the midplane is parallel to the infalling envelope streamlines. We therefore use this location as our footpoint for the cavity wall. Solutions close to this starting position quickly converge above the disk to the same surface; therefore, the exactness of the starting position is not critical for these models.

The left panel of Figure 1 plots the shape of the cavity scaled by r_d for a variety of values of Λ, while fixing $\lambda = 1/2$ (therefore

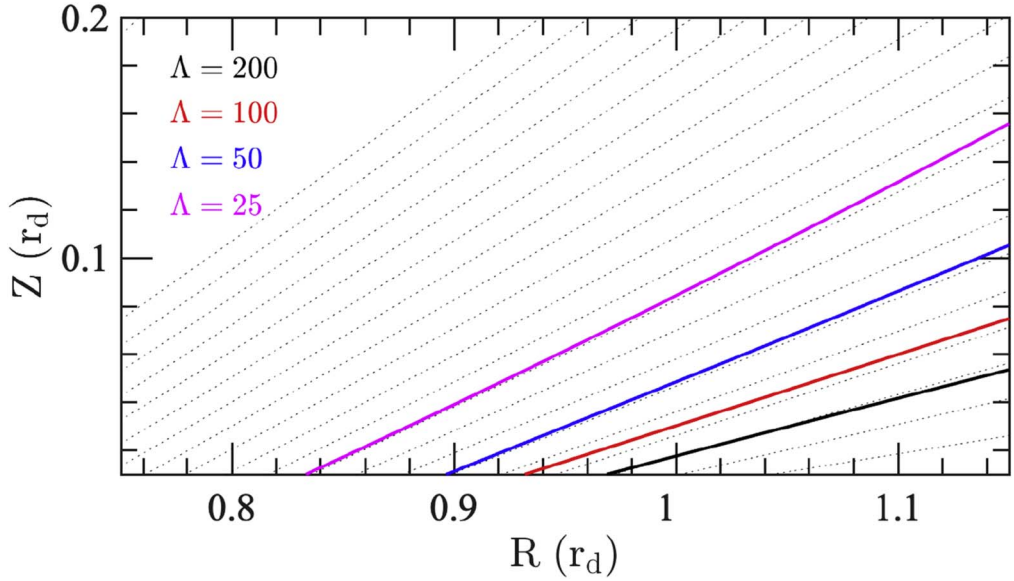

Figure 2. Cavity shapes near the base for an isotropic wind colliding with an Ulrich (1976) infalling envelope for fixed $\lambda = 1/2$ and varying Λ. The dashed lines represent streamlines for material flowing within the infalling envelope.

$\Lambda = \mathcal{M}_{\rm d}^2$). With this scaling, the envelope appears broadest and tallest when Λ is large due to the larger ratio of the ram pressure in the wind to the thermal pressure in the envelope at $r_{\rm d}$. As shown in the right panel of Figure 1, however, all solutions with different Λ values are self-similar away from the base and actually have identical physical sizes in units of $r_{\rm s}$ (defined in Equation (10)). The height of the cavity is found to be $Z_{\rm max} \sim 2.5\, r_{\rm s}$, while the maximum cylindrical radius of the cavity is $R_{\rm max} \sim 0.16\, r_{\rm s}$. It is important to note that the self-similarity of these solutions breaks down near the base, where the relevant scaling length remains $r_{\rm d}$ for all Λ.

The location and incidence angle at which the cavity intersects the midplane for all these solutions is set by requiring that the cavity interface be tangent to the infalling envelope streamlines. Figure 2 shows in detail the cavity shapes near the disk surface, as well as the orientation of the infalling streamlines from the envelope for the cases investigated in Figure 1. From the figure, it is clear that the smaller Λ solutions intersect the base somewhat interior to the larger Λ solutions. These solutions therefore result in less interaction with the infalling envelope, as can be seen in the figure by noting the trajectories of the envelope streamlines.

Until now we have fixed $\lambda = 1/2$; however, breakout solutions should exist for other values of λ. In Figure 3 we show the cavity shape for $\Lambda = 25$ and a variety of λ. At the base, the Λ solutions are *independent* of λ while the maximum cylindrical radius and height increase with increasing λ, quickly asymptoting to a fixed solution. Furthermore, in Figure 4 we plot, as a function of λ, both the maximum cylindrical radius $R_{\rm max}$ of the cavity (in units of $r_{\rm s}$) and the ratio of the height to the cylindrical radius at this widest point in the cavity for each of the Λ cases used in the previous figures. It is clear from these plots that for $\lambda > 1/2$, all the solutions become remarkably self-similar, with only a slight hint that the shapes are slightly broader for larger λ and smaller Λ. We further note that steady breakout solutions are found even for values of $\lambda < 1/2$ (down to $\lambda \simeq 0.2$). These solutions differ from the Mendoza et al. (2004) trapped solutions which are required a priori to have $\partial r/\partial\theta = 0$ along the vertical axis, creating a roundish "cap" strongly confined by infall ram pressure when $\lambda < 1/2$. Instead, our $0.2 \lesssim \lambda < 1/2$ cavities maintain flame-like shapes, such that the infall ram pressure at the tip is strongly reduced by the highly oblique incidence there and allows for breakout.

The fact that our numerical solutions are not highly dependent on the initial location of the interface at the disk surface (see Appendix A), nor on the exact values of λ or Λ, confirms that they are stable equilibrium solutions, as expected when the confinement is dominated by envelope pressure.

3. Flows along the Cavity Wall

The shape of the cavity wall as a function of the two defining input parameters (λ, Λ) was shown in Section 2 to be close to self-similar as long as $\lambda > 1/2$, especially at large distance from the intersection with the midplane. Thus, it is reasonable to expect that the flow of deflected material from either the wind or envelope side of the cavity wall can also be described in terms of a single simplified parameterization, with small deviations as a function of Λ due primarily to the slightly varying physical situation near the disk surface.

In order to keep track of the various flows, we divide the cavity wall surface into three components. We present a schematic of the various regions in Figure 5. First, there is the deflected shocked wind (denoted in the text by a subscript 1) that travels upward, parallel to and on the inside of the cavity surface. Second, there is the deflected infalling envelope (denoted in the text by a subscript 2), which travels downward, parallel to and on the outside of the cavity surface. In the absence of mixing across the surface, these two flows remain independent and can be fully described at each location by a mass and momentum flux explicitly determined by integration along the surface (see Equations (2)–(5) in Matsuyama et al. 2009). Third, a turbulent mixing layer (denoted in the text by the subscript L) in which slow-moving deflected envelope

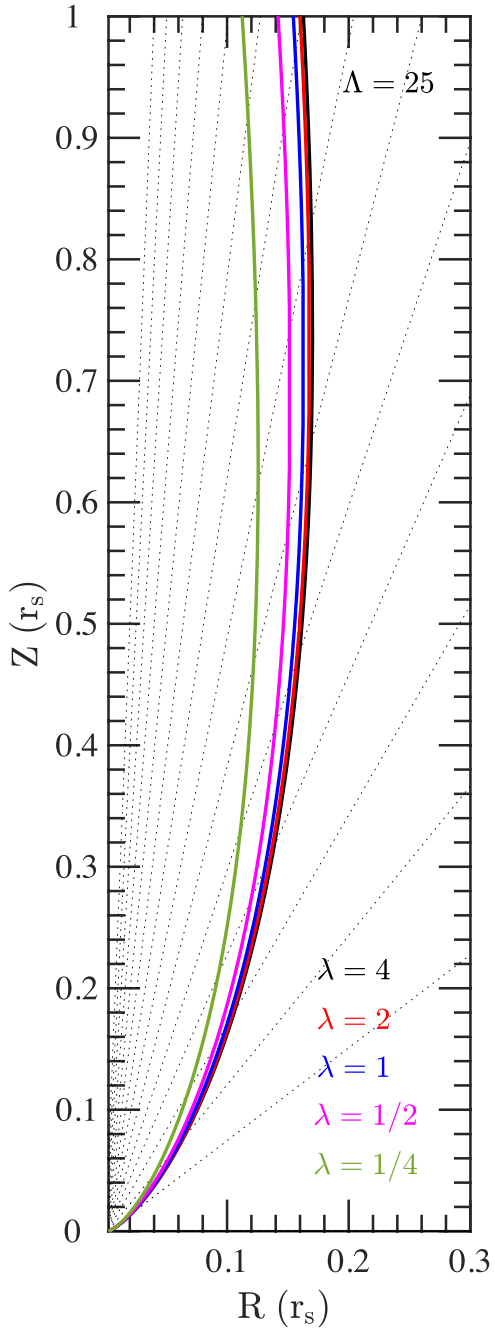

Figure 3. Cavity profiles for fixed $\Lambda = 25$ and varying λ showing breakout solutions when $\lambda > 0.2$. The dashed lines represent streamlines for material flowing within the infalling envelope onto the disk of radius $r_d = 2r_s/\Lambda^2$. As discussed in the text, in units of r_s the cavity shape becomes fixed for any Λ at large λ.

material is entrained upwards by the fast deflected wind can develop at the contact discontinuity between these two flows.

3.1. Solutions without a Mixing Layer

We begin with solutions in which there is no mixing between the upward and downward deflected flows. Figure 6 plots the mass flux as a function of (scaled) height for both the interior ($\dot{M}_1$; upward) and exterior ($\dot{M}_2$; downward) layers. The results are shown for a single hemisphere and scaled accordingly, as there is no explicit requirement within the model for symmetry about the disk plane. The right panel fixes $\lambda = 1/2$ and shows solutions for four values of Λ whereas the left panel fixes Λ and shows solutions for four values of λ. In these plots, it is important to recognize that the mass-flux axes are scaled separately, with the outflowing material $\dot{M}_1$ scaled to the total mass flux from the wind over a hemisphere and the infalling material $\dot{M}_2$ scaled to the mass infall rate from the envelope over a hemisphere. Thus, while all the solutions are self-similar well above the midplane, the relative importance of the upward versus downward mass flux depends on both λ and v_w/v_d (see Equation (8)). In all cases, the upward flowing surface asymptotes to the entire mass flux in the wind, as required, whereas the the cavity intercepts only a fraction of the infalling envelope, missing that part which lands on the disk surface between the cavity footpoint and r_d. The trend with Λ, seen in the right panel, can therefore be understood as a direct consequence of the fact that smaller Λ solutions intercept the disk closer to the central source (see Figure 2). As shown in the left-hand panel, all solutions at fixed Λ are approximately self-similar modulo the wind and infall mass flux scaling.

A similar set of solutions is found for the momentum flux as a function of height along the interior ($\dot{\Pi}_1 = \dot{M}_1 v_1$; outward) and exterior ($\dot{\Pi}_2 = \dot{M}_2 v_2$; inward) cavity layers, as shown in Figure 7. The quantities shown in the figure are scaled independently to the fiducial momentum flux in the wind and infalling material. The relative scaling between these quantities, however, is explicitly λ (see Equation (8)), and thus, it is apparent that the downward momentum flux in the outer layer is always much less than the upward momentum flux in the inner layer except extremely close to the base. The left-hand panel, again, shows that the solutions are approximately self-similar over a wide range of λ for fixed Λ.

Finally, the mean velocities (v_1, v_2) for the two deflected flows along the surface can be calculated directly from the ratio of the respective momenta and mass fluxes. These are plotted in Figure 8. The quantities shown in the figure are scaled independently to v_w and v_d. The wind typically intersects the surface at an acute angle and thus the majority of the momentum from the wind is deposited in the deflected flow rather than contributing ram pressure to support the surface against the infalling envelope. Therefore, the magnitude of the velocity of the deflected wind along the surface remains near v_w, asymptotically approaching v_w at large heights. The infalling envelope, however, is almost stationary at large distances from the midplane and thus the deflected material at large heights shows little movement downward along the surface. The infalling velocity increases dramatically near the base, deeper in the potential well of the central object, and thus the downward velocity within the deflected envelope increases toward the midplane. Note that the velocity v_2 along the external shell surface (deflected envelope) is always a tiny fraction of the upward velocity v_1 along the inner shell surface (deflected wind), as long as $v_w/v_d \gg 1$.

One more calculation is required in order to complete the analysis of the flows in the absence of partial entrainment. For consistency with the assumptions, it is necessary to show that the shocked wind and shocked envelope layers remain thin in comparison to the radius of the cavity. To accomplish this, we first determine the pressure confining the shocked layers (Figure 9). We note that on large scales the pressure may be

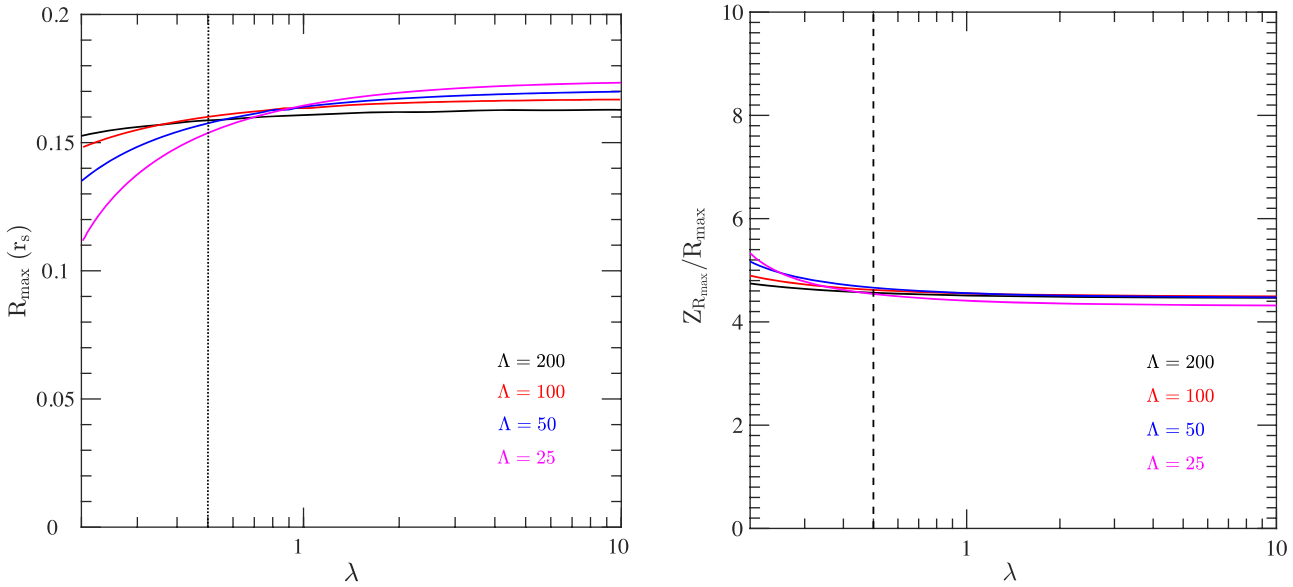

Figure 4. Left: maximum cylindrical radius, in units of r_s, for a cavity produced by an isotropic wind colliding with an Ulrich (1976) infalling envelope for a range of λ and Λ values. We find steady breakout solutions even when $\lambda < 1/2$, to the left of the dotted vertical lines. Right: ratio of the height of the cavity to the cylindrical radius of the cavity, measured at the location where the cavity is widest.

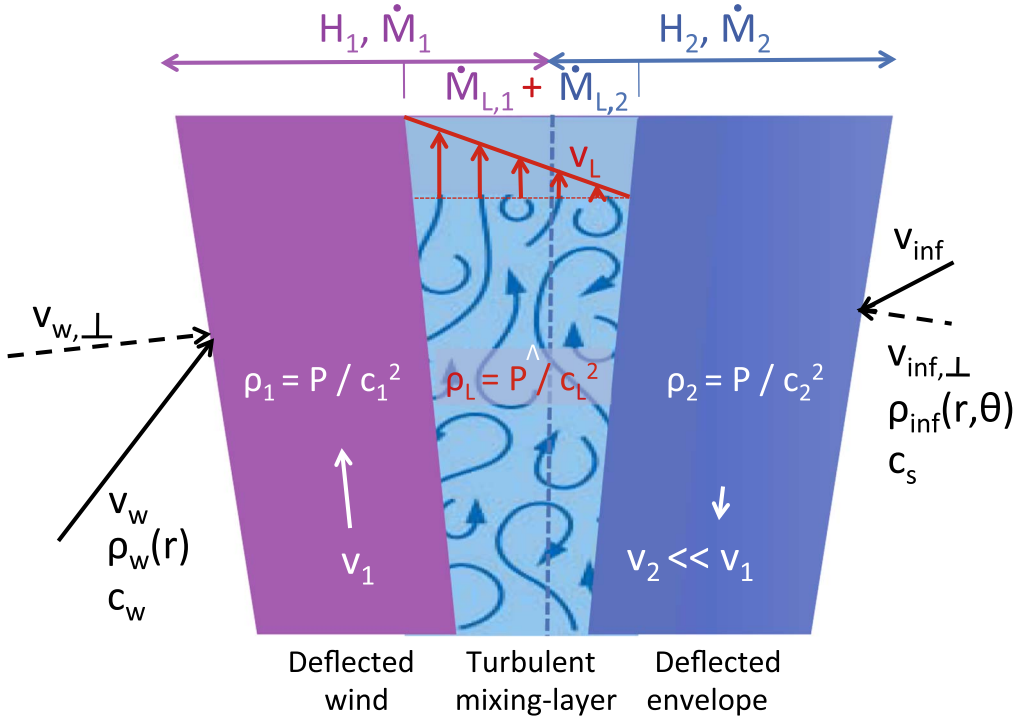

Figure 5. Schematic showing the various layers along the cavity wall, in which deflected wind material moves upward and deflected envelope material moves downward. A central turbulent mixing layer with a linear "Couette-type" velocity gradient may grow between these two layers (see Section 3.2). Mathematical notations used in the text for the velocity, mass flux, sound speed, and density in each part of the flow are also shown for easy reference.

well approximated by

$$P(Z) \simeq \left(\frac{\dot{M}_w v_w}{4\pi r_s^2}\right)\left(\frac{0.2 r_s}{Z}\right)^{1.5} \simeq 0.1\left(\frac{\dot{M}_w v_w}{4\pi r_s^{0.5}}\right) Z^{-1.5}. \quad (14)$$

Next, we compute the ratio of the thickness of the layers H_1 and H_2 against the radial extent of the cavity as a function of location along the cavity. In detail, the thickness of each deflected layer is equal to the surface density divided by the mass density within the layer. In the thin-shell approximation, the density within each layer is set by pressure equilibrium through $P = \rho_1 c_1^2 = \rho_2 c_2^2$, where $c_{1,2}$ are respectively the sound speed in the deflected wind and the deflected infalling envelope layer. Because P is proportional to the ram pressure from the wind, the scalings for the relative thickness of the two

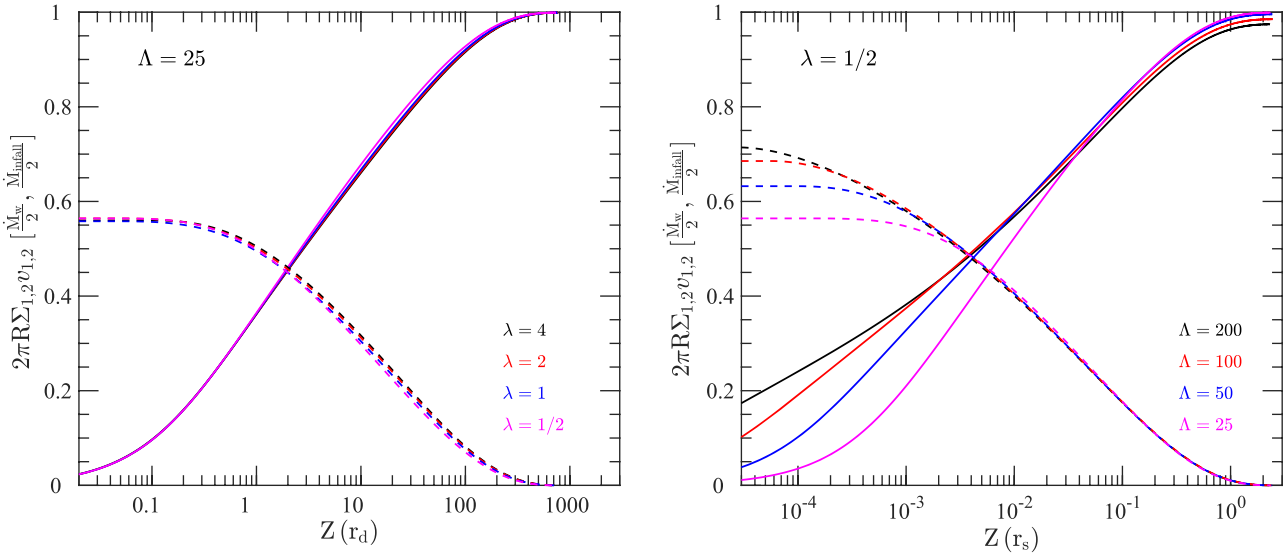

Figure 6. Mass flow along both the interior (upward: solid line) and exterior (downward: dashed line) layers. The solutions shown are for one hemisphere only. The y-axis is scaled independently for the downward and upward flows. The left panel shows the results with Z in units of $r_{\rm d}$ for a variety of λ while fixing $\Lambda = 25$. The right panel shows the results with Z in units of $r_{\rm s}$ for a variety of Λ while fixing $\lambda = 1/2$.

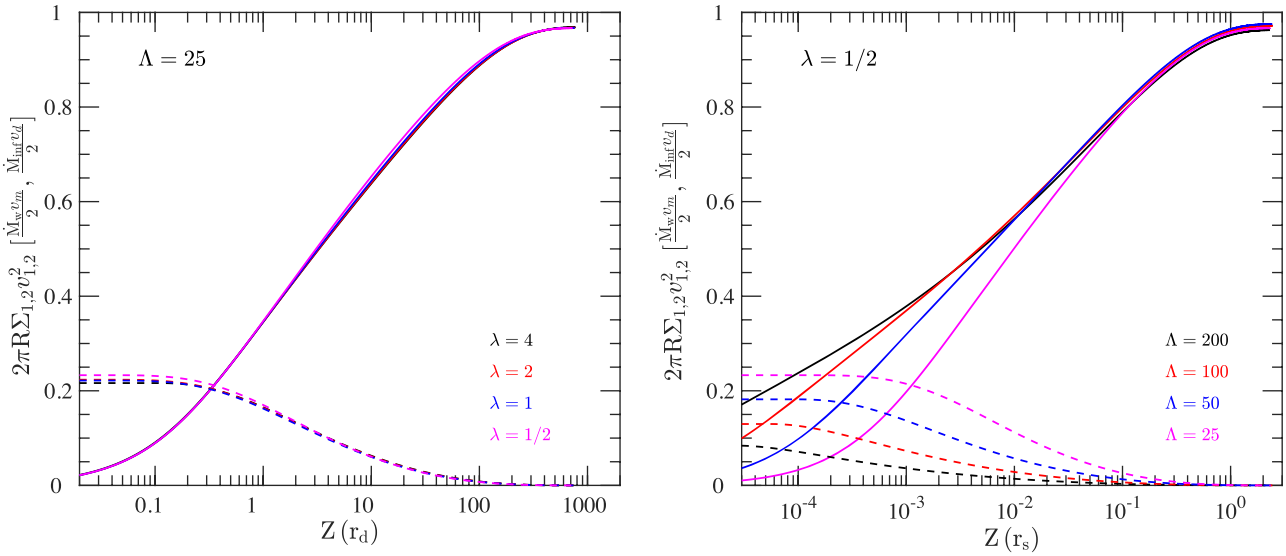

Figure 7. Momentum flow along both the interior (upward: solid line) and exterior (downward: dashed line) layers. The solutions shown are for one hemisphere only. The y-axis is scaled independently for the downward and upward flows. The left panel shows the results with Z in units of $r_{\rm d}$ for a variety of λ while fixing $\Lambda = 25$. The right panel shows the results with Z in units of $r_{\rm s}$ for a variety of Λ while fixing $\lambda = 1/2$.

deflected layers simplify to

$$\frac{H_1}{R} \propto \left(\frac{\dot{M}_{\rm w}}{v_{\rm w}}\right)\left(\frac{\dot{M}_{\rm w} v_{\rm w}}{c_1^2}\right)^{-1} \propto \left(\frac{v_{\rm w}}{c_1}\right)^{-2} \tag{15}$$

and

$$\frac{H_2}{R} \propto \left(\frac{\dot{M}_{\rm inf}}{v_{\rm d}}\right)\left(\frac{\dot{M}_{\rm w} v_{\rm w}}{c_2^2}\right)^{-1} \propto \left(\frac{c_{\rm s}}{c_2}\right)^{-2} \Lambda^{-1}. \tag{16}$$

Figure 10 presents the relative thickness H/R of the two layers, normalized by their respective relevant scaling in each case. Except near the top of the cavity, where the solution converges back toward the axis of rotation, the deflected wind and envelope layers remain thin provided $v_{\rm w}/c_1 > 10$ and $\Lambda\,(c_{\rm s}/c_2)^2 > 10$, respectively. Furthermore, Figure 8 shows that the deflected wind suffers oblique shocks with speed $v_{\rm s} = v_{\rm w,\perp} \simeq 0.2\,v_{\rm w}$. Using the general expression for the maximum temperature reached behind a hydrodynamical shock of speed $v_{\rm s}$ to set an upper limit on c_1, it may then be determined that the condition for the shocked wind layer to remain thin is equivalent to $v_{\rm w}/c_{\rm w} > 10$, with $c_{\rm w}$ the isothermal sound speed in the wind.

Similarly, Figure 8 also shows that the deflected envelope undergoes only small velocity jumps $v_{\rm s} = v_{\rm inf,\perp} < 0.1 v_{\rm d}$. Because we will always have $c_2 \geqslant c_{\rm s}$, a conservative condition ensuring that the deflected envelope layer will remain thin, regardless of the value of $v_{\rm d}$, is simply that $\Lambda > 10$. This conservative condition on Λ becomes unnecessary, however, if $v_{\rm d}$ is large enough for the velocity jumps to remain supersonic everywhere along the cavity wall. Using the expression for the

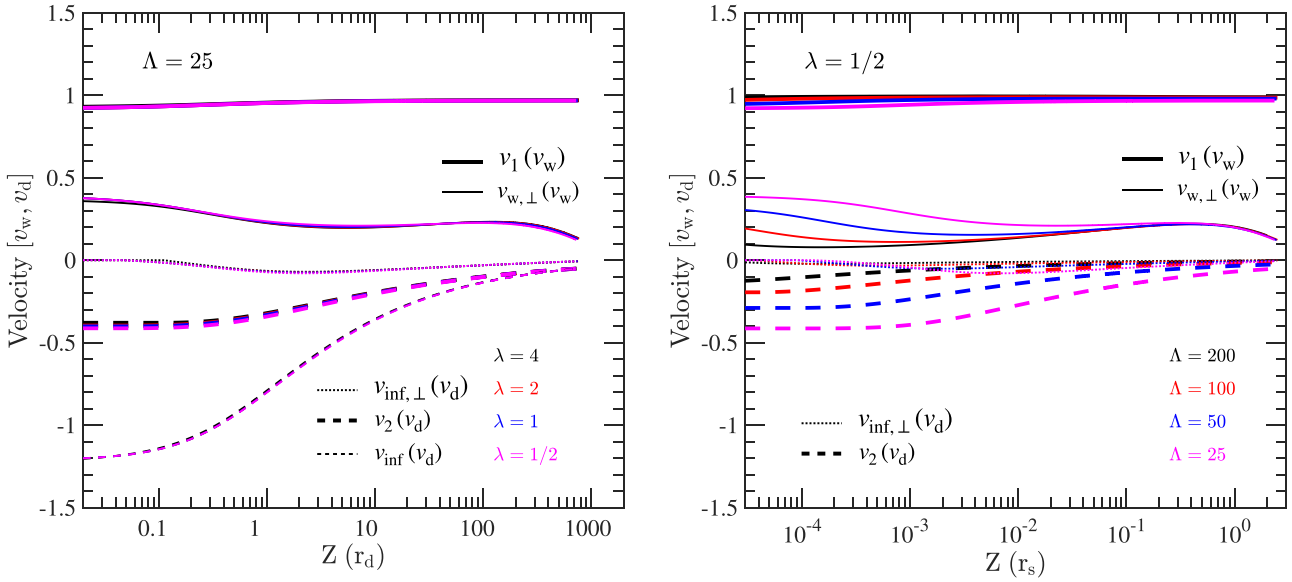

Figure 8. Mean velocity along both the interior (upward: top two lines) and exterior (downward: bottom lines) layers. The solutions shown are for one hemisphere only. The *y*-axis is scaled independently for the upward and downward flows. The left panel shows the results for a variety of λ while fixing $\Lambda = 25$ with Z in units of $r_{\rm d}$ while the right panel shows the results for a variety of Λ while fixing $\lambda = 1/2$ with Z in units of $r_{\rm s}$.

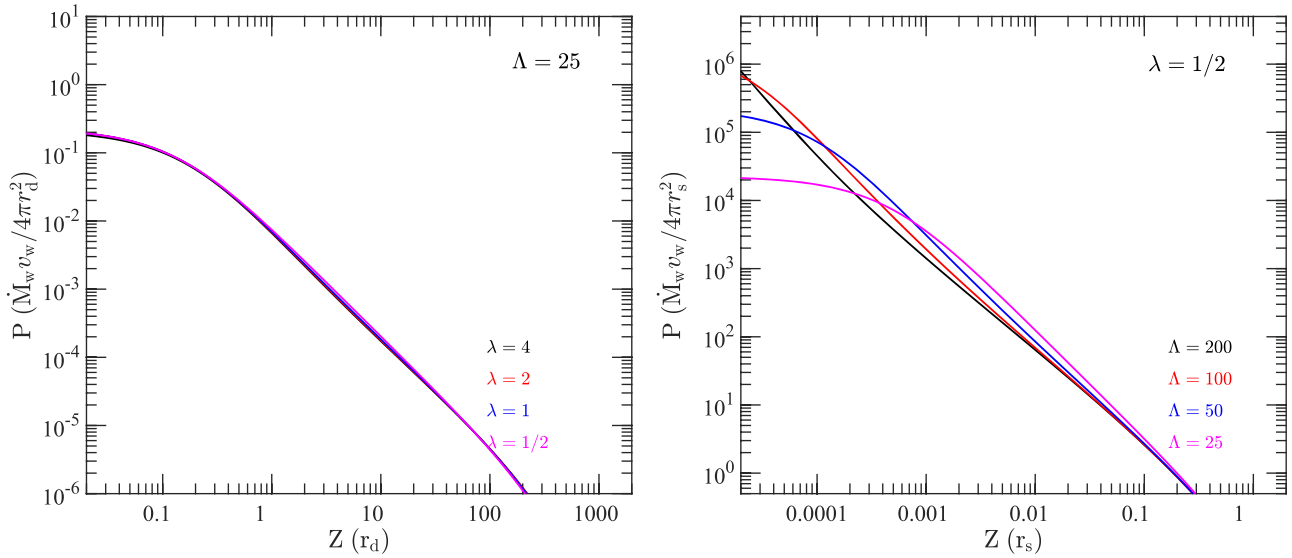

Figure 9. Normalized pressure along the boundary surface of the cavity. The left panel shows the results for a variety of λ while fixing $\Lambda = 25$ with Z in units of $r_{\rm d}$. The right panel shows the results for a variety of Λ while fixing $\lambda = 1/2$ with Z in units of $r_{\rm s}$.

maximum temperature behind a shock at $v_{\rm s}$ to set an upper limit on c_2, and rewriting the condition for a thin envelope layer as $\lambda > 5\,(c_2/v_{\rm d})^2$ (using Equation (12)), we find that the inequality is then automatically fulfilled under our wind breakout condition $\lambda > 0.2$, regardless of the value of Λ.

The combined results presented in Figures 6–10 reveal that, in the absence of mixing, the deflected wind mass flowing upward along the boundary surface will be similar to the total mass flowing in the wind, $\dot{M}_{\rm w}$, and that the magnitude of the momentum in this deflected flow will also be close to the wind momentum flux $\dot{M}_{\rm w} v_{\rm w}$.

Due to the large aspect ratio of the cavity, the bulk of the deflected wind flows roughly perpendicular to the disk and at a high velocity, $v_1 \sim v_{\rm w}$. Alternatively, if mixing takes place between the momentum-rich outward-flowing layer and the mass-rich infalling layer, the internal velocity structure of this turbulent mixing layer should be significantly differentiated, as for example, through a linear velocity gradient such as occurs in a Couette flow (e.g., Raga et al. 1995). Such an occurrence will naturally produce a wider spread of velocities between v_2 and v_1.

3.2. Solutions with a Mixing Layer

A general formalism for the growth of a turbulent mixing layer between two axisymmetric flows was derived by Raga et al. (1995). Their main formulae included some ambiguities and typographical errors, and are therefore reproduced in corrected form in Appendix B. These authors assume that within the mixing layer there is both a fixed temperature, referred to by its sound speed $c_{\rm L}$ and a fixed pressure P across

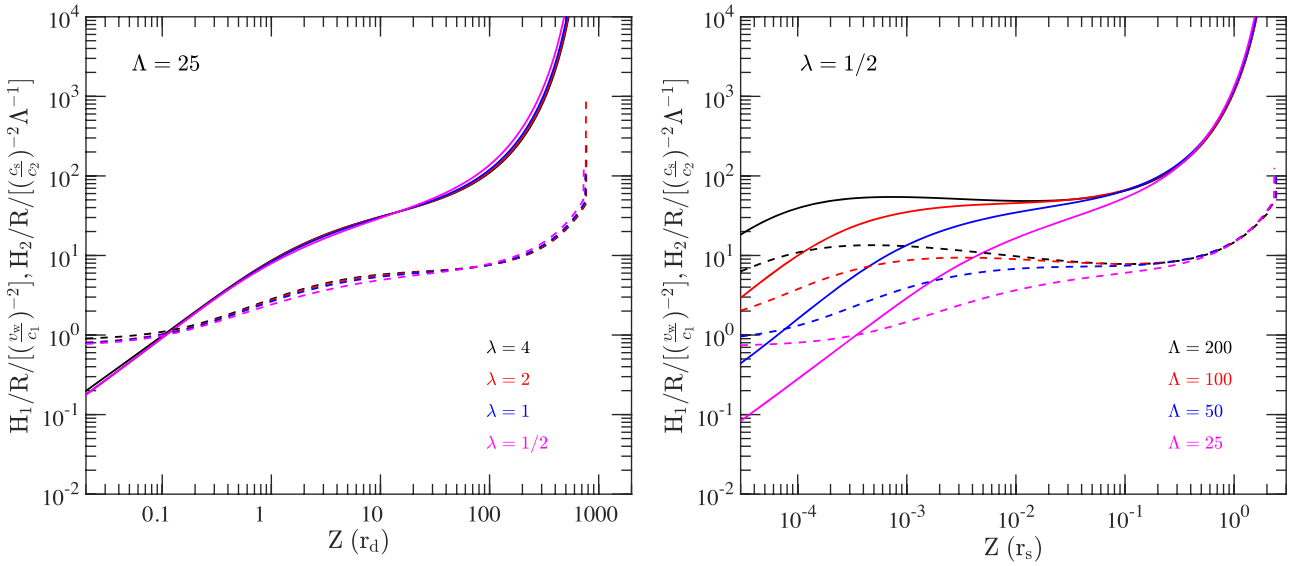

Figure 10. Relative thickness of both the interior (upward: solid line) and exterior (downward: dashed line) layers as a function of height. The ratio H/R is normalized in each case to the relevant scaling derived in Equations (15) and (16). The left panel shows the results for a variety of λ with Z in units of r_d while fixing $\Lambda = 25$. The right panel shows the results for a variety of Λ with Z in units of r_s while fixing $\lambda = 1/2$.

the layer, varying only as a function of position along the flow. Across the layer, they further assume that the velocity varies linearly, as in a Couette flow, bounded by the velocities of the fast v_1 layer and slow v_2 layer (see Figure 5). The coupled equations for the change in mass flux and momentum flux within the mixing layer due to entrainment across the inner and outer boundaries are then solved so as to determine the entrainment required across each bounding surface in order to maintain the imposed Couette conditions.

As detailed by Raga et al. (1995), entrainment occurs in two ways (see their Equations (1) and (2)): through the geometrical growth of the mixing layer, intercepting a fraction of the flows on either side, and through "turbulent entrainment" on the slow-moving side (here the deflected envelope) as it is dragged into the mixing layer by the fast-moving side. In this paper, we follow the Raga et al. (1995) prescription for the turbulent entrainment velocity $v_{ent} = \alpha c_2^2/c_L$ (see their Equation (3)), with a constant turbulent mixing parameter α. For simplicity, we will further assume constant values of c_L, c_1, and c_2 at all positions.

At any location x along the surface, the linear velocity gradient across the turbulent layer ensures that the mass-weighted mean velocity within the mixing layer is $\overline{v_L}(x) = [v_1(x) + v_2(x)]/2$. At the same time, the ratio of the momentum flux $\dot{I}_L$ versus the mass flux $\dot{M}_L$ in the mixing layer is skewed toward the higher velocities within the layer, such that

$$\frac{\overline{v_L^2}}{\overline{v_L}} \equiv \frac{\dot{I}_L(x)}{\dot{M}_L(x)} = \frac{2}{3}\left(\frac{v_1^3(x) - v_2^3(x)}{v_1^2(x) - v_2^2(x)}\right). \quad (17)$$

To maintain this ratio as slow envelope material $\dot{M}_{L2}$ is turbulently entrained across the outer boundary surface, a significant amount of fast-flowing shocked wind material $\dot{M}_{L1}$ must also be entrained across the inner boundary, with the exact proportion set by the (changing) physical conditions along the surface. For the trivial case of a constant velocity, v_1, in the fast-moving layer and no motion on the slow-moving side ($v_2 = 0$), Equation (17) shows that the Couette flow requires $\dot{I}_L(x) = (2v_1/3)\dot{M}_L(x)$. Because zero momentum can be provided from the stationary side, this condition is met by the mass entrainment rate from the fast-moving wind side being exactly twice the mass entrainment rate from the stationary side (Cantó & Raga 1991).

A careful consideration of the interface solutions presented in Section 2 shows that for the self-similar cavities in this paper, $v_1 \sim v_w$ and $|v_2| \ll v_w$ in all examined cases. This simplifies the general formulae described by Raga et al. (1995); however, the changing radius of curvature and the steadily dropping pressure across the calculated wind–envelope surface conspire such that the detailed solution for entrainment must be calculated numerically and separately for all parameter pairs (λ, Λ). Fortunately, despite this somewhat more complicated geometry, Figure 11 shows that for all pairs (λ, Λ), the mass flux entering the mixing layer from the fast-flowing wind side, $\dot{M}_{L1}$, remains close to twice the turbulent entrainment from the envelope side, $\dot{M}_{L2}$.

The self-similarity of the boundary location also provides, for each (λ, Λ) pair, a scaling relation for the efficiency of the turbulent mixing solutions in terms of the physical parameters $\dot{M}_w$, v_w, c_L, as well as α. The turbulent entrainment into the mixing layer from the slow-moving, envelope, side of the boundary, $\dot{M}_{L2}$, can be found by integrating the turbulent entrainment along the boundary surface, x. That is,

$$\dot{M}_{L2} = 2\pi \int R(x)\rho_2(x)v_{ent}\, dx, \quad (18)$$

where $\rho_2(x)$ is the density of the deflected shocked envelope along the outer boundary and $v_{ent} = \alpha(c_2^2/c_L)$ is the parameterized entrainment velocity. This equation is exact for situations where the shocked ambient medium is static and remains an excellent estimate when $|v_2| \ll v_w$. The result may be rewritten in terms of the pressure across the boundary surface

$$\dot{M}_{L2} = 2\pi\left(\frac{\alpha}{c_L}\right)\int R(x)P(x)dx, \quad (19)$$

which is further reduced by recognizing that the pressure at location x along the surface is set explicitly by the ram

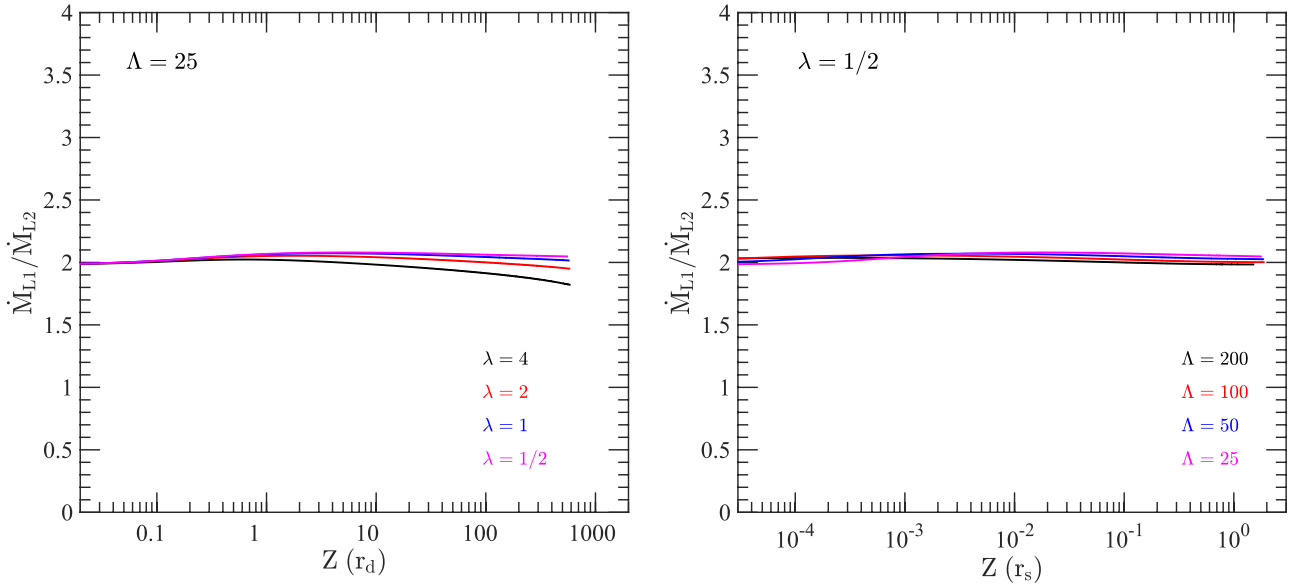

Figure 11. Computed ratio of the mass flux entrained within the mixing layer from the fast-moving shocked wind material, $\dot{M}_{\rm L1}$, vs. the turbulent entrainment from the shocked envelope, $\dot{M}_{\rm L2}$. Note that for all solutions the ratio remains close to 2, as expected to maintain a linear Couette velocity profile across the mixing layer.

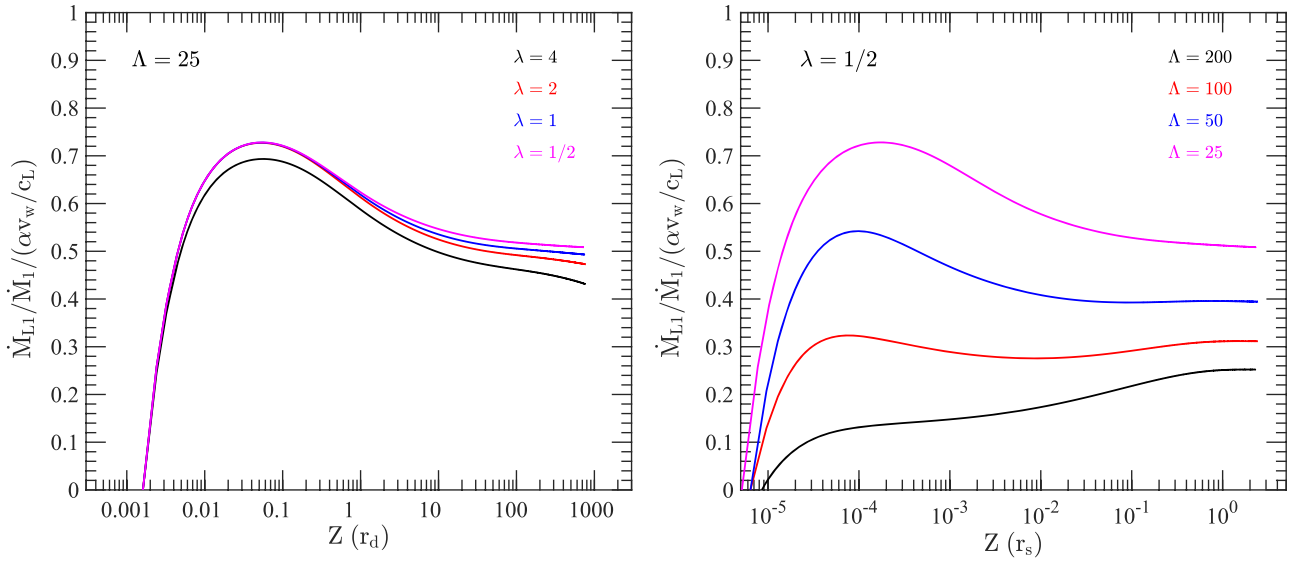

Figure 12. Computed ratio of the cumulative material gained by the mixing layer from the shocked wind ($\dot{M}_{\rm L1}$) vs. the available reservoir of shocked wind material including that already in the mixing layer.

pressure: $P(x) = a(x)\dot{M}_{\rm w} v_{\rm w}$, where $a(x) \propto \sin^2\gamma/r^2$ takes into account the varying angle of incidence between the isotropic wind and the boundary surface. Thus,

$$\dot{M}_{\rm L2} = 2\pi\left(\frac{\alpha\ \dot{M}_{\rm w}\ v_{\rm w}}{c_{\rm L}}\right)\int R(x)a(x)dx. \qquad (20)$$

Furthermore, given the almost fixed ratio between mass entrained into the mixing layer from the deflected wind versus the deflected envelope (see Figure 11), the scaling for $\dot{M}_{\rm L1}$, and $\dot{M}_{\rm L} = \dot{M}_{\rm L1} + \dot{M}_{\rm L2}$, should be the same as that for $\dot{M}_{\rm L2}$.

Utilizing this scaling as normalization, Figures 12 and 13 show the fraction of deflected wind and deflected envelope that is entrained into the mixing layer as a function of height above the midplane, for a variety of (λ, Λ) pairs. Self-consistent solutions require that these fractions remains less than unity, otherwise the reservoir of shocked material flowing along the cavity walls is not large enough to feed material into the mixing layer at our assumed rates. From Figure 12, it is clear that for the wind side this constraint requires

$$\alpha \lesssim \alpha_{\rm max} \equiv \left(\frac{c_{\rm L}}{v_{\rm w}}\right). \qquad (21)$$

Similarly, for the envelope side (Figure 13), the constraint is trivially met for the same physical parameters assuming $\dot{M}_{\rm w} < 0.5\dot{M}_{\rm inf}$, except at extreme heights, $Z > r_{\rm s}$, where the cavity shape converges to the axis of rotation.

Furthermore, combining the information in Figures 12 and 13, and using the results of Figure 6, Figure 14 shows that the total mass flux in the mixing layer for one outflow cavity lobe

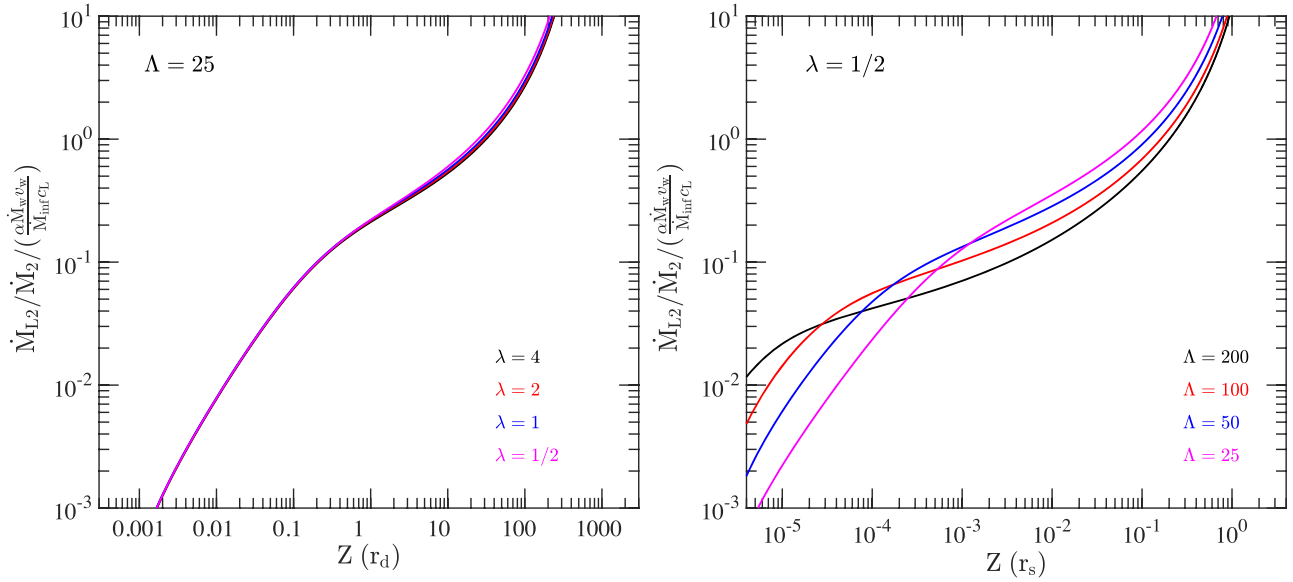

Figure 13. Computed ratio of the cumulative material gained by the mixing layer from the deflected envelope ($\dot{M}_{\rm L2}$) vs. the available reservoir of deflected envelope material including that already in the mixing layer.

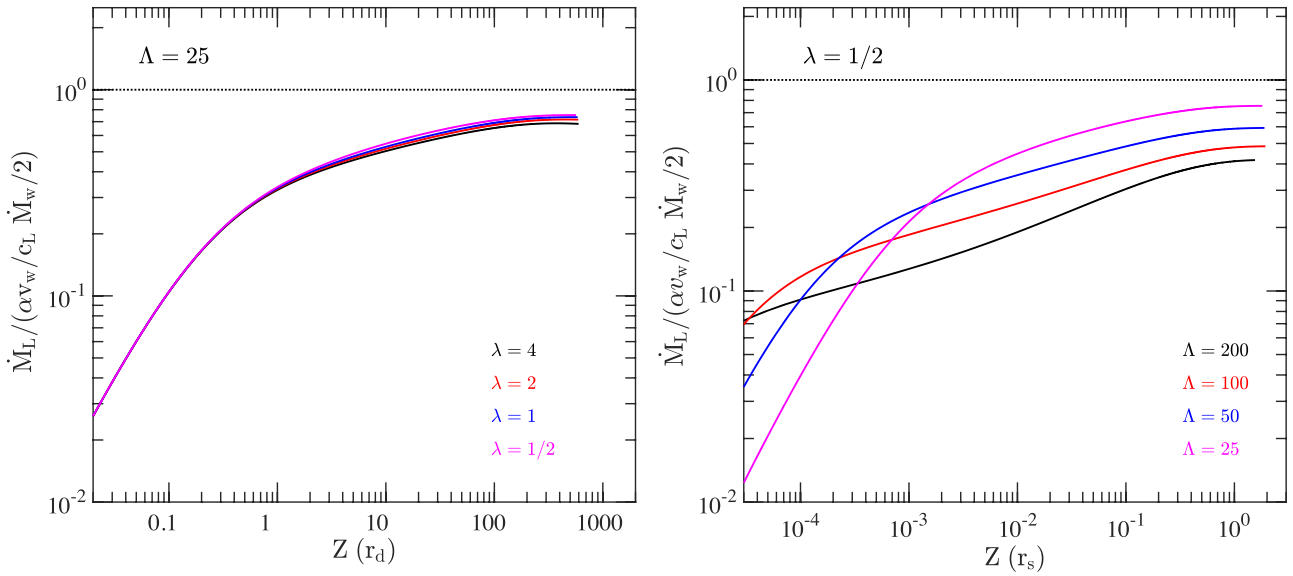

Figure 14. Mass flux of the material within the mixing layer.

is almost independent of the (λ, Λ) pair. Within a factor of a few, the asymptotic value at high altitudes is

$$\dot{M}_{\rm L} \sim \left(\frac{\alpha\, v_{\rm w}}{c_{\rm L}}\right)\frac{\dot{M}_{\rm w}}{2} = \left(\frac{\alpha}{\alpha_{\rm max}}\right)\frac{\dot{M}_{\rm w}}{2}, \tag{22}$$

where $\alpha_{\rm max}$ is defined in Equation (21). We note that if $\alpha > \alpha_{\rm max}$, our physical model will not entirely break down. The mixing layer will simply grow until it eventually engulfs all of the deflected wind layer and $\dot{M}_{\rm L}$ saturates at its maximum possible value of $\dot{M}_{\rm w}/2$. Without a fast laminar wind layer to enforce a Couette flow, however, the velocity field in the mixing layer would become a Gaussian velocity distribution peaked around a mean value $\simeq v_{\rm w}/2$, leading to line profiles much narrower than in a linear gradient Couette flow.

4. Calculation of Angular Momentum and Line Profiles

4.1. Angular Momentum of the Shocked Envelope and Mixing Layer

To compute the angular velocity of the shocked envelope, $v_{2,\phi}$, as well as the mixing layer, $v_{{\rm L},\phi}$, we adopt the following equations (see Equation (5) in Matsuyama et al. 2009):

$$\rho_{\rm inf}(v_{\rm inf}\sin\theta_{\rm sa})\Omega_{{\rm inf},\phi} = \frac{\cos\beta}{R^3}\frac{\partial}{\partial R}(R^3\Sigma_2 v_2\Omega_{2,\phi}) \tag{23}$$

and

$$\rho_2(\alpha c_2)\Omega_{2,\phi} = \frac{\cos\beta}{R^3}\frac{\partial}{\partial R}(R^3\Sigma_{\rm L} v_{\rm L}\Omega_{{\rm L},\phi}), \tag{24}$$

where $\Omega_{2,\phi} = v_{2,\phi}/(2\pi R)$ and $\Omega_{{\rm L},\phi} = v_{{\rm L},\phi}/(2\pi R)$.

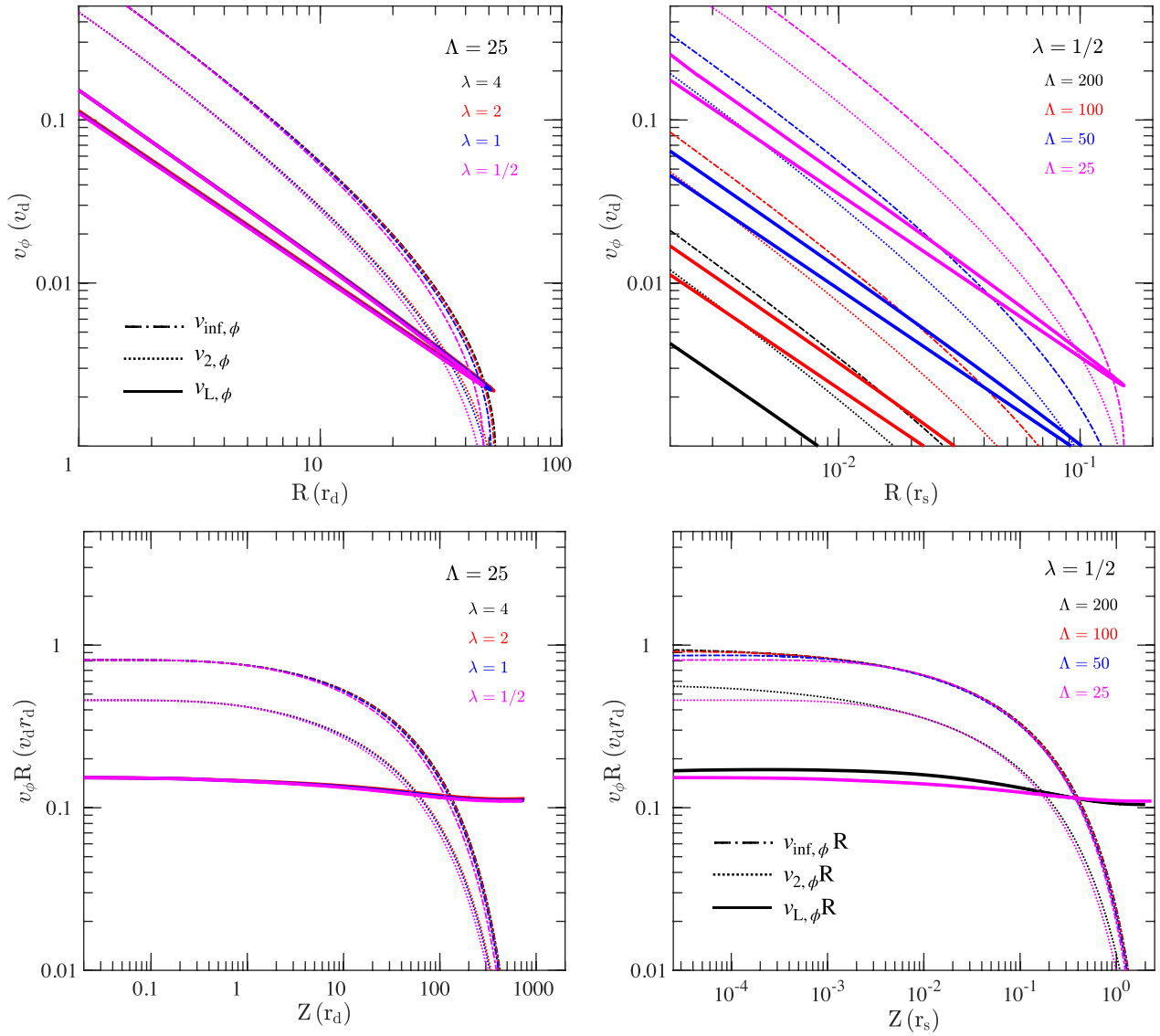

Figure 15. The ϕ component of the infalling envelope at the interface (dotted–dashed), in the shocked envelope gas (dotted) and in the gas within the central mixing layer (solid). The top panels plot velocity while bottom panels plot specific angular momentum. The left panels compare the results for fixed $\Lambda = 25$ and varying λ with R in units of $r_{\rm d}$. The right panels compare results for fixed $\lambda = 1/2$ and varying Λ with R in units of $r_{\rm s}$.

By integrating Equation (23) over R along the interface from the top of the cavity to the disk plane, we obtain $\Omega_{2,\phi}$ and hence $v_{2,\phi}$. Subsequently, inputting the derived $\Omega_{2,\phi}$ into Equation (24) and integrating it over R from the disk plane upward along the interface, we obtain $\Omega_{\rm L,\phi}$ and hence $v_{\rm L,\phi}$. In the top panels of Figure 15, we show $v_{\rm L,\phi}$ (solid lines), $v_{2,\phi}$, and $v_{\rm inf,\phi}$ as a function of R for fixed Λ and varying λ (left panels), as well as for fixed λ and varying Λ (right panels). We can see that for $\Lambda > 20$, $v_{\rm L,\phi}$ is no larger than a few tenths of $v_{\rm d}$ and therefore can be considered as negligible compared to the bulk velocity of the gas in the mixing layer ($v_{\rm L} \approx 0.5\, v_{\rm w}$) when determining the shell shape and computing the observed line profiles.

The bottom panels of Figure 15 plot the specific angular momentum Rv_ϕ for the same three velocity components as in the upper panels, as a function of Z. We can see that the specific angular momentum in the mixing layer is virtually independent of λ and Λ. Because twice as much material is entrained from the (nonrotating) wind side than from the envelope side, the initial value of the specific angular momentum at the base is one-third of that in the deflected envelope. As gas is advected upwards in the mixing layer, this rotating material gets mixed with deflected ambient material of smaller specific angular momentum. However, because most of the mass entrainment occurs at $Z \leqslant 0.1\, r_{\rm s}$, the specific angular momentum in the mixing layer remains close to its initial value, $\simeq 0.15\, v_{\rm d} r_{\rm d}$.

4.2. Mixing-layer Line Profile

Having developed a model for how the material is entrained, the next step is to calculate the resulting line profile for direct comparison to observations. The model calculations in the preceding sections were all dimensionless and are thus applicable to essentially any type of entrainment irrespective of physical scale. Thus, with the appropriate scaling, this model could be compared with outflows from protostars (e.g., Mottram et al. 2014; Kristensen et al. 2017) to extragalactic outflows (e.g., Aalto et al. 2016, 2017).

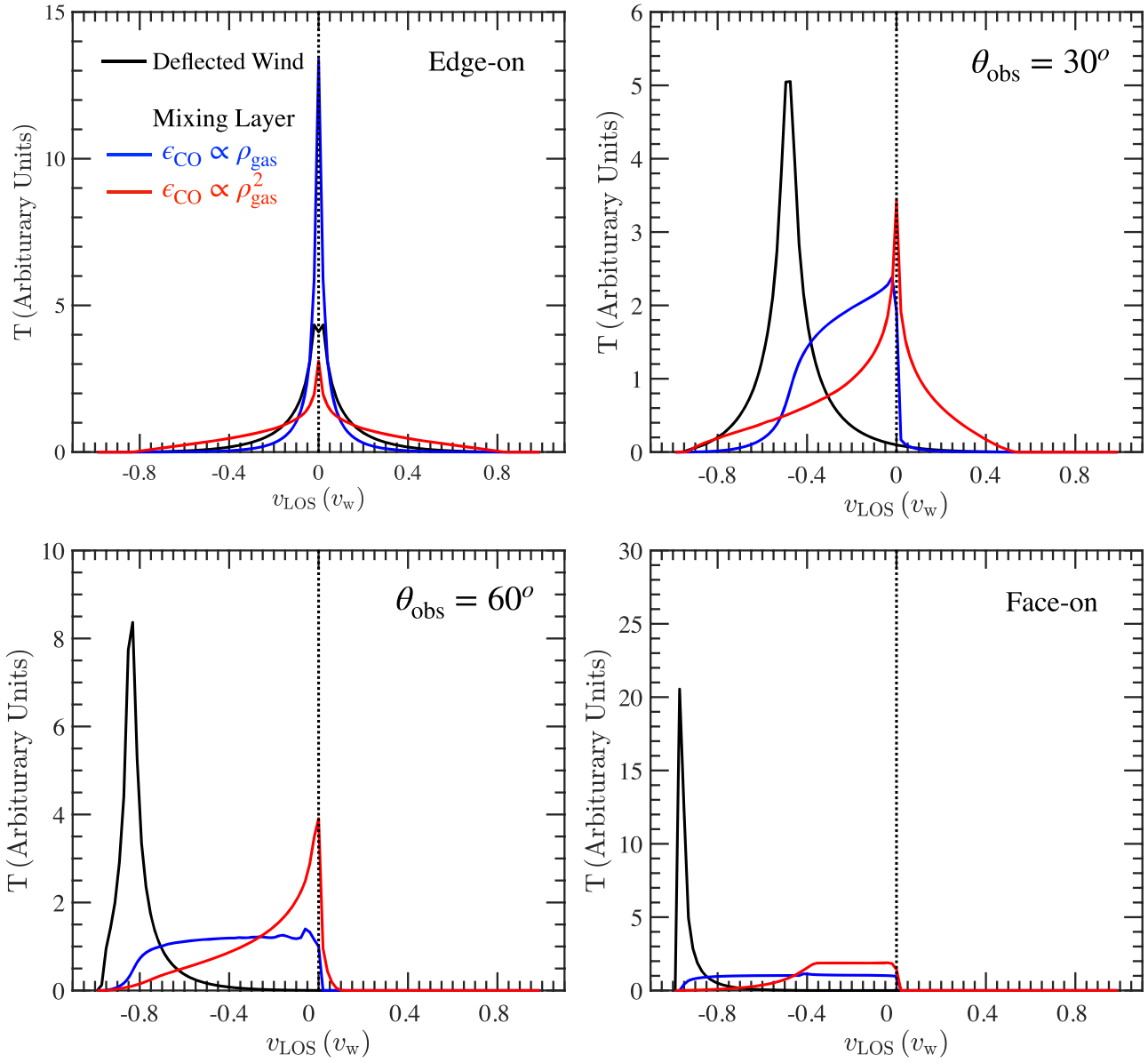

Figure 16. Line profiles for the model with $\Lambda = 25$ and $\lambda = 1/2$. Each panel shows the result for a different direction of viewing as labeled, where θ_{obs} is measured from the plane of the disk. The blue and red curves in each panel indicate the line profiles of material in the mixing layer, under the assumption that the emissivity of CO $J =$ 16—15 (ϵ_{CO}) is proportional to the density and square of the density, respectively. For reference, we also show in each panel the emission profile of the material in the shocked wind layer alone if no entrainment occurs, under the assumption that emissivity scales linearly with gas density (black curve).

The line profiles for the shocked wind layer and for the turbulent mixing layer are generated independently under the optically thin assumption by computing the flux $dF_e(v_{LOS}) = \epsilon_e dV$ emitted by each elementary volume element dV, where ϵ_e is the emissivity per unit volume of the molecular line of interest. At every height, z, along the surface, the flux from each azimuthal interval, $d\phi$, is added to the velocity bin corresponding to the line-of-sight velocity v_{LOS} of the volume element. For the shocked wind layer, the velocity has a unique modulus v_1, dependent only on z, whereas for the mixing layer, the flux is evenly distributed in velocity between 0 and v_1 prior to projection.

In Figure 16, we show example line profiles for our reference model presented in the previous section ($\lambda = 1/2$, $\Lambda = 25$). We scale the projected velocities by v_w and integrate the emission up to $200r_d$ ($0.6r_s$) from the base of the outflow. Four viewing angles are provided. The black curves show the line profiles for the shocked wind layer only, assuming emissivity proportional to density—mimicking the high-density LTE (local thermodynamic equilibrium) regime. Except for the edge-on case, the emission always peaks near the projected wind velocity $v_w \sin \theta_{obs}$. This occurs because the bulk of the deflected wind flows at $v_1 \sim v_w$ and is roughly parallel to the disk axis, due to the elongated shape of the cavity. The blue curves, on the other hand, show the computed line profiles for the mixing layer only, assuming again that the emissivity is proportional to the density. As expected, the line profiles are much broader and flatter, peaking at zero and extending to a fraction of v_w. Finally, the solid red curves show the predicted line profiles from the mixing layer when emissivity is proportional to the density squared, mimicking the low-density limit. This emissivity condition increases the contribution of dense regions near the base, where the cavity opening angle is

still large. Due to projection effects, it produces more extended line wings close to edge on and enhanced low-velocity emission when close to pole on.

Our described model of partial entrainment of the wind, along with some of the exterior envelope, through a turbulent mixing layer thus ensures that a fraction of the outflowing material is moving slowly due to the linear velocity gradient, Couette-type flow within the mixing layer. Turbulent dissipation within the mixing layer also provides a heating mechanism to make this material warmer than the shocked wind layer and hence brighter in high-J CO lines.

In the following section, we investigate whether such a model could explain at the same time the line profile, momentum, and temperature of the broad component observed in CO by Herschel toward the Serpens-Main SMM1 protostar, as well as the observed outflow cavity size, for reasonable envelope and wind parameters.

5. Application to the Broad Component of Class 0 Protostar Serpens-Main SMM1

As an illustration of the applicability of our formalism to a specific outflow case, we compare our model predictions with observations of the protostar Serpens-Main SMM1. This protostar is located in the Serpens Main cloud at a distance of 438 pc (Herczeg et al. 2019). The protostar has a bolometric luminosity of $\sim$100 $L_\odot$ (Goicoechea et al. 2012), and is therefore on the border between low- and intermediate-mass protostars. The envelope is correspondingly massive, with an estimated mass of $\sim$50 $M_\odot$ (Enoch et al. 2008; Kristensen et al. 2012). When observed at high angular resolution, the protostar breaks up into multiple sources; however, the central, most massive protostar is responsible for the primary outflow (Hull et al. 2016, 2017; Le Gouellec et al. 2019). When observed in H_2O and high-J CO emission with the HIFI instrument on Herschel, this source shows the brightest line intensity in H_2O and CO J = 16–15 in the sample of Kristensen et al. (2017). For this reason, the broad-line component of SMM1 also has the highest signal-to-noise ratio. Hence, this protostar is a natural choice for a first comparison between the model presented in this paper and observational data.

5.1. Broad Component Line Profile and Wind Velocity

When Herschel-HIFI started observing H_2O emission toward protostars, one of the biggest surprises was that the velocity-resolved line profiles typically were dominated by a broad outflow component with an FWHM of $\gtrsim$30 km s^{-1} (e.g., Kristensen et al. 2012, 2017; Mottram et al. 2014). This line width was significantly larger than seen in low-J CO from the ground, e.g., J = 3–2, where the FWHM is $\lesssim$15 km s^{-1} (Kristensen et al. 2012). It also became clear that when observing higher-J CO transitions with HIFI, the line profiles started resembling the H_2O profiles so much so that the CO J = 16–15 profiles are indistinguishable from the H_2O profiles (Kristensen et al. 2017). That the CO profiles vary with excitation suggests that the change in shape is indeed due to excitation as opposed to chemistry. Furthermore, the change in profile shape is likely related to an increase in temperature, because when calculating the rotational temperature from the ratio between CO lines, the temperature increases from $\lesssim$100 K to $\sim$300 K (Yildiz et al. 2013; Kristensen et al. 2017). Thus, the higher-J CO lines, and by implication the similar H_2O lines, trace a warmer, faster-moving component of the protostellar outflow as compared to what is seen in low-J transitions (Kristensen et al. 2017), and this component is primarily seen as a broad outflow component in the velocity-resolved line profiles.

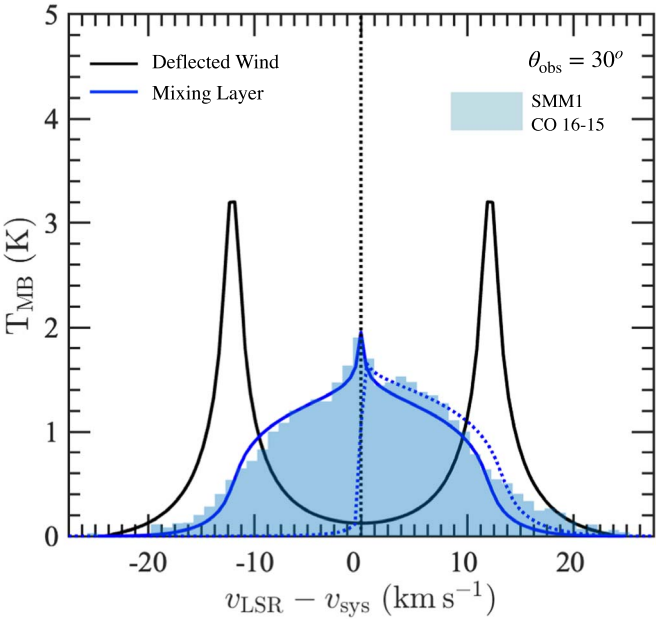

Figure 17. Observed broad component of the CO J = 16–15 line profile in SMM1 (filled blue) compared against synthetic line profiles produced in Section 4. The synthetic profiles are generated at a viewing angle θ_{obs} = 30° from the disk plane, with an emissivity that scales linearly with gas density. The blue and black curves assume that the CO emission originates from the central mixing layer or from the deflected wind layer, respectively. The solid profiles include both outflow lobes and are rescaled to v_w = 25 km s^{-1} so that the blue line can well match the left side of the observed SMM1 profile. An additional blue dotted fit is provided for the redshifted lobe (right side) of the SMM1 profile, requiring a somewhat larger v_w = 28 km s^{-1}.

Kristensen et al. (2012) and Mottram et al. (2014) speculated that, because of the higher temperature and velocity, this broad component is tracing gas closer to a shock front, possibly located where the protostellar wind shocks against the infalling envelope in an irradiated C-type shock. The colder gas, traced by lower-J CO lines, then would be the subsequently entrained swept-up ambient gas. Alternatively, the heating and entrainment process of the broad component could take place within a turbulent mixing layer at the interface between the shocked wind and infalling envelope. This alternate scenario is investigated below, using the model results presented in the previous sections.

For the source SMM1, Kristensen et al. (2017) found that the CO J = 16–15 line profile could be decomposed into three Gaussian components, one broad (FWHM $\sim$ 20 km s^{-1}) and two narrower components (FWHM $\sim$ 8–10 km s^{-1}). The narrower components are only seen in this high-J CO line and likely originate in shocks very close to the protostar (Kristensen et al. 2013), and they are not considered further here. Figure 17 compares the broad component, extracted from the CO J = 16–15 line profile in SMM1 by Kristensen et al. (2017) after removal of the two narrower component Gaussian fits, with our model predictions. Excellent agreement is found for a mixing layer with v_w = 25–30 km s^{-1}, an inclination of θ_{obs} = 30° measured from the plane of the disk, and an emissivity proportional to density.

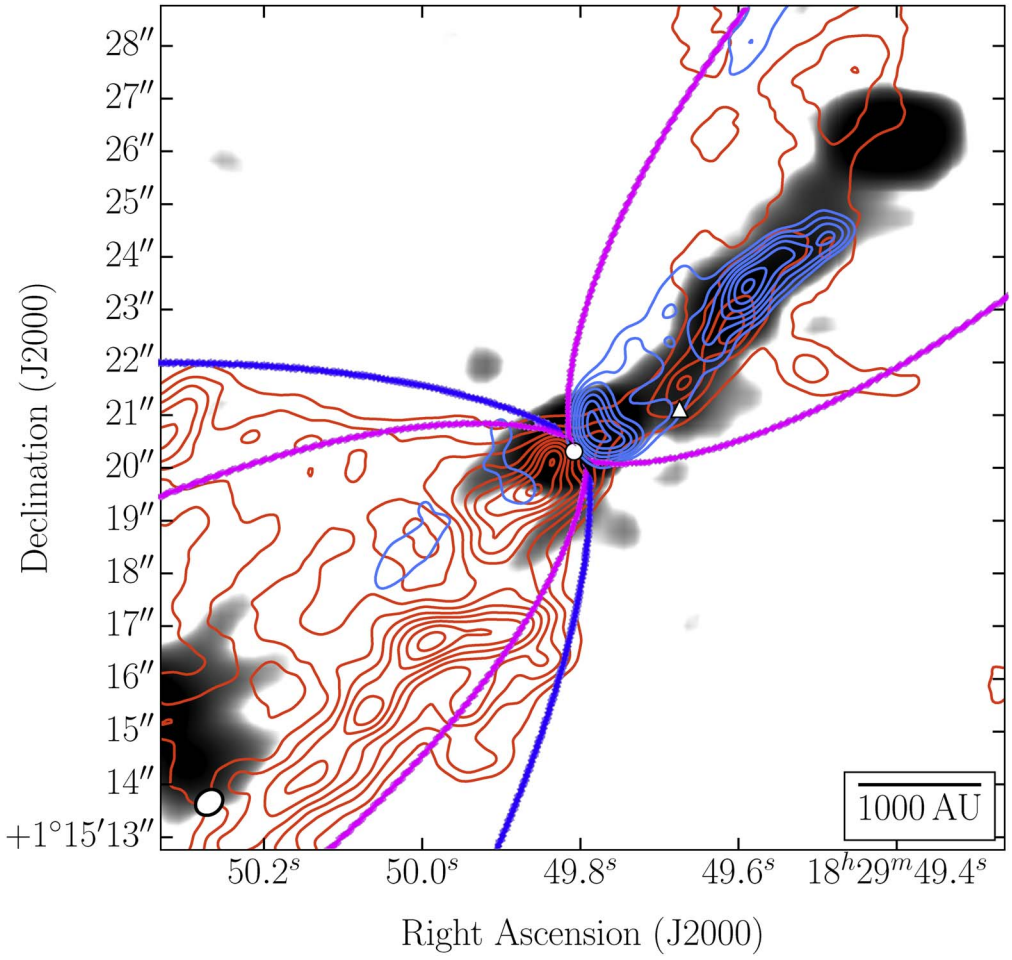

Figure 18. Model cavity shapes superimposed onto the observed CO map from Hull et al. (2016). The magenta and blue lines correspond to $\Lambda = 25$ and $\Lambda = 50$ in our model, respectively (see Figure 1). They have been rescaled to $r_s = 10{,}000$ au (magenta) and $r_s = 40{,}000$ (blue) in order to match the observed CO map profile.

A few checks are in order to ensure that the model remains self-consistent. First, for the "thin-shell" approximation to be satisfied, the wind velocity must remain large enough to produce a significant ram pressure which in turn confines the flow of shocked wind along the cavity surface. In Section 3.1, we showed that confinement requires $v_w/c_w > 10$, where c_w is the isothermal sound speed in the wind. With our estimate for $v_w \simeq 30\ \mathrm{km\,s^{-1}}$, we therefore require $c_w < 3\ \mathrm{km\,s^{-1}}$, or a maximum wind temperature of $1000\,\mu$ K, with μ the mean molecular weight per particle (in a.m.u). This condition holds both in D-winds heated by ambipolar diffusion in Class 0 sources (Panoglou et al. 2012; Yvart et al. 2016) and in X-winds in the absence of mechanical heating (Shang et al. 2002). In Section 3.1, we also found that the deflected envelope layer will always remain thin when $\Lambda > 10$, regardless of the value of v_d. We will verify that this condition holds in SMM1 in Section 5.5.

Second, the model line profiles in blue that reproduce the observed line profile shape for SMM1 in Figure 17 are obtained only if a Couette linear velocity gradient exists across the mixing layer. For this gradient to be maintained, the mass flow entrained in the mixing layer from the wind side, $\dot{M}_{L1}$, should not exhaust the available flux of shocked wind material $\dot{M}_l$ flowing along the shell. As discussed in Section 3.2, this constraint sets an upper limit on the turbulent entrainment coefficient in SMM1 $\alpha \leqslant \alpha_{max} = (c_L/v_w) \simeq 0.035$ (see Equation (21) and Figure 12) where we have used our estimate of $v_w = 25$–$30\ \mathrm{km\,s^{-1}}$ from line profile modeling and $c_L = 1\ \mathrm{km^{-1}}$ from the temperature ≃250 K inferred by multiline CO analysis of the broad component in SMM1 (see Kristensen et al. 2017 and the next section). We will verify below that this upper limit on α is still compatible with the observed momentum in the broad component of SMM1.

5.2. Outflow Cavity Size

In Figure 18, we compare a published CO outflow map of SMM1 (Hull et al. 2016) with our predicted self-similar cavity shape from Figure 1 for various values of the scaling parameter r_s. Although only the inner region of the SMM1 outflow has been mapped at high angular resolution, the joint constraints on small and large scales indicate that r_s must lie in the range ≃10,000–40,000 au. Hence, we adopt $r_s = 20{,}000$ au as our fiducial value in the following.

The cavity physical scale r_s requires a specific ratio of mass-loss rate in the wind to infall rate in the envelope (see Equation (10)), given by

$$\frac{\dot{M}_w}{\dot{M}_{inf}} = \frac{c_s^2}{v_w}\left(\frac{r_s}{2GM_\star}\right)^{0.5} \simeq 0.035\left(\frac{c_s}{0.4\ \mathrm{km\ s^{-1}}}\right)^2 \times \left(\frac{30\ \mathrm{km\ s^{-1}}}{v_w}\right)\left(\frac{r_s}{20{,}000\ \mathrm{au}}\right)^{1/2}\left(\frac{0.2\,M_\odot}{M_\star}\right)^{1/2}. \quad (25)$$

Because SMM1 is quite bright (100 $L_\odot$), we adopt a fiducial sound speed in the envelope of $c_s \simeq 0.4$ km s^{-1} corresponding to a temperature of 40 K. This value is consistent with radiative-transfer modeling of the dust emission from the envelope surrounding SMM1 (Kristensen et al. 2012), which recovers a sound speed of 0.3–0.5 km s^{-1} in the envelope at the relevant physical scales, 350–3000 au, shown in Figure 18, which are also those of the Herschel/HIFI beam. With this value of c_s, we find that the observed size of the outflow cavity in SMM1 can be reproduced with a wide-angle wind mass flux on the order of 4% of the envelope infall rate, which is quite modest. In the following sections, we use our model and the observed momentum in the broad component to constrain the absolute value of $\dot{M}_w$ and then that of $\dot{M}_{inf}$, through Equation (25).

5.3. Momentum in the Mixing Layer

The two-sided momentum in the broad component of SMM1 was estimated from observations of CO $J = 3$–2, 6–5, 10–9, and 16–15 taken with the JCMT, APEX, and Herschel-HIFI (Yildiz et al. 2013). The respective line profiles were rebinned to the same velocity scale and to channels of 3 km s^{-1} width. For each channel, a rotational diagram was constructed, and, assuming LTE and optically thin emission, the rotational temperature and CO column density N_{CO} were calculated. The rotational temperature was ~250 K, irrespective of velocity. With this mass spectrum in place, the mass-weighted momentum Π_{BC} of the broad component summed over both lobes is given by

$$\Pi_{BC} = \pi R_b^2 \left(\frac{1.4 m_H}{X_{CO}}\right) \int N_{CO}(v)|v|\, dv \equiv \Pi_{obs}\left(\frac{5\times10^{-5}}{X_{CO}}\right), \quad (26)$$

where X_{CO} is the (unknown) fractional abundance of CO molecules by number with respect to H nuclei in the broad component and Π_{obs} is the fiducial "observed" momentum assuming a standard interstellar CO abundance of 5×10^{-5}. Equation (26) shows that the value of Π_{obs} only depends on the observed CO intensity and excitation temperature, irrespective of the true X_{CO}. It is therefore the quantity usually reported in observational papers. Using an updated distance, $d = 438$ pc, to the Serpens Main cloud (Herczeg et al. 2019), we recalculate the Yildiz et al. (2013)-derived fiducial momentum inside a beam radius of $R_b = 5''.5 = 2400$ au to be $\Pi_{obs} \simeq 8 \pm 2 \times 10^{-2} M_\odot$ km s^{-1}.

In our entrainment model, the two-sided momentum contained in the mixing layer up to a distance $z = \pm R_b$ is given by

$$\begin{aligned} 2\Pi_L &= 2\times\int_0^{R_b} dz \int_0^h \rho_L(h,z) v_L(h,z) 2\pi R(z) dh \\ &= 2\times\int_0^{R_b} \dot{M}_L(z) dz \\ &= \dot{M}_w\left(\frac{\alpha v_w}{c_L}\right)\times\int_0^{R_b}\eta(z)dz \simeq \dot{M}_w\left(\frac{\alpha}{\alpha_{max}}\right)\times\eta_b R_b, \end{aligned} \quad (27)$$

where $\eta(z)$ is the normalized ratio plotted in Figure 14 and α_{max} is defined in Equation (21). Because $\eta(z)$ increases very slowly with height, the integral on z may be approximated as $\eta_b R_b$, where $\eta_b \equiv \eta(R_b)$.

If the momentum in the broad component of SMM1 inside $R_b = 2400$ au is provided by mixing-layer entrainment from a wide-angle wind, then $2\Pi_L = \Pi_{BC}$. Using Equation (26) with $\Pi_{obs} \simeq 8 \pm 2 \times 10^{-2}\, M_\odot$ km s^{-1} and taking $\eta_b \simeq 1$ (which we will verify in Section 5.5), we infer that the wide-angle wind must have a mass flux

$$\begin{aligned} \dot{M}_w &= \left(\frac{\alpha_{max}}{\alpha}\right)\left(\frac{\Pi_{BC}}{\eta_b R_b}\right) \\ &\simeq 6\times10^{-6}\left(\frac{\alpha_{max}}{\alpha}\right)\left(\frac{5\times10^{-5}}{X_{CO}}\right) M_\odot\ \mathrm{yr}^{-1}. \end{aligned} \quad (28)$$

5.4. Infall Rate

We can now compute the required envelope infall rate in our model and compare it with the infall rate independently suggested by dust envelope models. Combining Equations (25) and (28), we infer the required infall mass flux to reproduce both the outflow cavity size and the momentum in the broad component to be

$$\begin{aligned} \dot{M}_{inf} &= \dot{M}_w\left(\frac{\dot{M}_{inf}}{\dot{M}_w}\right) \\ &\simeq 1.4\times10^{-4}\, M_\odot\ \mathrm{yr}^{-1}\left(\frac{\alpha_{max}}{\alpha}\right) \\ &\quad\times\left(\frac{5\times10^{-5}}{X_{CO}}\right)\left(\frac{M_\star}{0.2M_\odot}\right)^{1/2}. \end{aligned} \quad (29)$$

The required value is larger than typical infall rates for low-mass Class 0 protostars. It is in line, however, with that expected for sources with particularly massive envelopes such as SMM1, whose luminosity ~100 $L_\odot$ places it on the border between low- and intermediate-mass protostars. Using the estimated H_2 density at 1000 au, n_{1000}, in the SMM1 dust envelope model of Kristensen et al. (2012) and rescaling by d^2 from $d = 230$ to 438 pc, we infer an "observed" envelope infall rate at $R_{1000} = 1000$ au of

$$\begin{aligned} \dot{M}_{env} &= 4\pi R_{1000}^2\, n_{1000}\, v_{inf}(R_{1000}) \times (1.4 m_{H_2}), \\ &\simeq 1.7\times10^{-4}\, M_\odot\ \mathrm{yr}^{-1}\left(\frac{n_{1000}}{1.5\times10^7 \mathrm{cm}^{-3}}\right)\left(\frac{M_\star}{0.2M_\odot}\right)^{1/2}, \end{aligned} \quad (30)$$

where the factor of 1.4 accounts for the mass in the form of Helium. We note that $M_\star$ appears at the same power in $\dot{M}_{inf}$ and $\dot{M}_{env}$, hence its exact value, currently unknown in SMM1, does not matter for the comparison. There is therefore good agreement with our mixing-layer model as long as X_{CO}, the CO abundance in the mixing layer with respect to H nuclei, is close to the standard interstellar value of 5×10^{-5}, and the turbulent entrainment parameter α is close to the maximum value to maintain a Couette flow, $\alpha_{max} = c_L/v_w \simeq 0.03$. We note that such a value of α matches very well with a model fit to supersonic mixing-layer experiments[6]; thus, it appears

[6] Cantó & Raga (1991) showed that the variation of opening angle versus Mach angle in experiments could be reproduced with $\epsilon \equiv v_{ent}/c_2 = 0.089\epsilon_2$ with $\epsilon_2 \equiv c_2/(3c_L)$; this is equivalent to our adopted prescription $v_{ent} = \alpha c_2^2/c_L$ with $\alpha \simeq 0.03$.

physically plausible. With these values for X_{CO} and α, the wind mass flux that is required to provide the broad component momentum is $\dot{M}_w \simeq 6 \times 10^{-6} M_\odot$ yr^{-1} (see Equation (28)).

5.5. Constraints on Ejection/Accretion Ratio and Disk Radius

We have shown in Section 5.2 that the outflow cavity size in SMM1 can be reproduced with a modest ratio of wind mass flux to envelope infall rate of ≃4%. The disk accretion rate onto the central star, however, may be smaller than the envelope infall rate onto the disk. Assuming that the bolometric luminosity ≃100$L_\odot$ of the SMM1 source (Goicoechea et al. 2012) is dominated by the accretion luminosity $L_{acc} \simeq GM_\star \dot{M}_{acc}/R_\star$ and adopting stellar radii $R_\star$ on the birth line computed by Hosokawa & Homukai (2009), we infer a disk accretion rate of $\dot{M}_{acc} \simeq 10^{-4}\, M_\odot$ yr^{-1} if $M_\star = 0.2\, M_\odot$ and $\dot{M}_{acc} \simeq 3 \times 10^{-5}\, M_\odot$ yr^{-1} if $M_\star = 0.5\, M_\odot$. With the wide-angle wind mass flux $\dot{M}_w \simeq 6 \times 10^{-6} M_\odot$ yr^{-1} derived in the previous section, the ratio of wind ejection rate to disk accretion rate is thus ≃0.06–0.2 for $M_\star = 0.2$–$0.5 M_\odot$. Such values are in the typical range predicted by D-wind and X-wind ejection models from accretion disks around young stars. Therefore, the wind mass-flux requirements in our model for SMM1 appear physically reasonable.

We next estimate the expected range of the parameter λ, the ratio of wind to infall ram pressure, for SMM1. From Equations (8) and (10), we have

$$\lambda = \frac{v_w \dot{M}_w}{v_d \dot{M}_{inf}} = \left(\frac{c_s^2}{GM_\star}\right)\sqrt{\frac{r_s \times r_d}{2}} \simeq 0.5\left(\frac{r_s}{20{,}000\ \mathrm{au}}\right)^{1/2}\left(\frac{r_d}{30\ \mathrm{au}}\right)^{1/2} \times \left(\frac{c_s}{0.4\ \mathrm{km\ s^{-1}}}\right)^2\left(\frac{0.2\, M_\odot}{M_\star}\right). \quad (31)$$

This is consistent with the condition $\lambda \gtrsim 0.2$ for which our cavity solutions break out and reach their full extent (see Figure 4), for the typical disk sizes in Class 0 sources (Maury 2019). Interferometric continuum observations suggest that SMM1 possesses a particularly large and massive disk of ≃300 au (Enoch et al. 2009), hence the breakout condition is very likely fulfilled.

Finally, we estimate the typical Λ parameter as

$$\Lambda = \sqrt{\frac{2r_s}{r_d}} = 36 \times \left(\frac{r_s}{20{,}000\ \mathrm{au}}\right)^{1/2}\left(\frac{30\ \mathrm{au}}{r_d}\right)^{1/2}. \quad (32)$$

This low value of Λ is consistent with our assumption of $\eta_b \simeq 1$ on the scale $z = R_b \simeq 0.1 r_s$ of the Herschel beam (see the curves for $\eta(z)$ in the right panel of Figure 14). Even with a large disk, $r_d \simeq 300$ au, the condition $\Lambda > 10$ for the weakly shocked deflected envelope layer to remain thin is also fulfilled.

5.6. Temperature and Density in the Mixing Layer

As an additional test of our model, we investigate whether the observed temperature $T_L \simeq 250$ K of the broad component in SMM1 suggested by multiline CO analysis (Kristensen et al. 2017) would be consistent with the heating of the mixing layer in our model by turbulent viscosity.

In principle, a full nonequilibrium thermochemical calculation should be performed as a function of position along the mixing layer. Such a complex problem is, however, outside the scope of the present paper and is deferred to future work. For simplicity, we assume here that the temperature and chemistry in the mixing layer have reached a steady state on the scales observed by the Herschel-HIFI beam and check whether thermal equilibrium at $T_L \simeq 250$ K could indeed be sustained.

Following Binette et al. (1999), we take a turbulent viscosity $\mu = (\alpha/4)\rho_L c_L h$, with h the total thickness of the mixing layer. A derivation of this expression for supersonic isothermal mixing layers with a linear velocity profile (Couette flow) is given in Appendix C. We can then express the turbulent heating rate per unit volume in the mixing layer as

$$\Gamma_{visc} = \mu\left(\frac{dv}{dh}\right)^2 = \left(\frac{\alpha \rho_L c_L}{4h}\right) v_w^2 = \left(\frac{\alpha v_w}{c_L}\right)\left(\frac{P v_w}{4h}\right) = \left(\frac{\alpha/\alpha_{max}}{2\dot{M}_L}\right)\pi R\ P\ \rho_L\ \overline{v_L} v_w, \quad (33)$$

where we make use of $(dv/dh) = v_w/h$ with $h = \dot{M}_L/(2\pi R \rho_L \overline{v_L})$, R is the local shell radius, $P = \rho_L c_L^2$ is the local pressure in the layer, and $\alpha_{max} = c_L/v_w$ is defined in Equation (21).

Thermal equilibrium at constant T_L will be maintained as long as

$$\Gamma_{visc} \simeq \Lambda_{exp} + \Lambda_{rad}, \quad (34)$$

where Λ_{exp} is the rate of "expansion cooling" in the mixing layer as the pressure P drops with altitude and Λ_{rad} is the radiative cooling rate (both per unit volume). The contribution of H_2 formation is ignored in this analysis, as well as the advection of thermal energy into the layer, because $c_1 \ll v_w$ and $c_2 \ll v_w$. Under our isothermal hypothesis for the mixing layer, the expansion cooling rate may be simply expressed as

$$\Lambda_{exp} = -\frac{dP}{dt} = \overline{v_L}\left(\frac{-dP}{dx}\right) = \overline{v_L}\left(\frac{P}{x}\right)\left(\frac{-d\log P}{d\log x}\right), \quad (35)$$

where x denotes the position along the layer. We thus obtain

$$\frac{\Lambda_{exp}}{\Gamma_{visc}} = \left(\frac{\alpha_{max}}{\alpha}\right)\frac{4h}{x}\left(\frac{\overline{v_L}}{v_w}\right)\left(\frac{-d\log P}{d\log x}\right) = 2\dot{M}_L\left(\frac{\alpha_{max}}{\alpha}\right)\left(\frac{1}{\pi R x \rho_L v_w}\right)\left(\frac{-d\log P}{d\log x}\right) = \eta(z)\left(\frac{\dot{M}_w\, v_w}{P(z) 4\pi r_s^2}\right)\left(\frac{4r_s^2}{Rx}\right)\left(\frac{c_L}{v_w}\right)^2\left(\frac{-d\log P}{d\log x}\right), \quad (36)$$

where η is the normalized mass flux within the mixing layer plotted in Figure 14. Therefore, in our model, the ratio of expansion cooling to viscous heating in the mixing layer is independent of the turbulent entrainment efficiency α, and it only scales with $(c_L/v_w)^2$. Furthermore, the remaining terms in this ratio are only weakly dependent on the values of λ and Λ (see Figures 9 and 14). On the typical scale $z \leqslant 0.1\, r_s$ encompassed by the Herschel/HIFI beam, we find that $(\Lambda_{exp}/\Gamma_{visc}) \leqslant 200 (c_L/v_w)^2$. With our fitted values of $c_L \simeq 1$ km s^{-1} and $v_w \simeq 30$ km s^{-1} for the broad component of

SMM1, we infer that expansion cooling should be negligible with respect to viscous heating.

Thus, we only need to compare the viscous heating rate with the radiative cooling rate. As noted by Kristensen et al. (2017; see their Figure 11), cooling by CO largely dominates over the cooling by H_2 at temperatures of 250 K (for a standard CO/H_2 abundance ratio). We further assume that CO cooling is excited mainly by collisions with H_2 in the low-density limit (which we will verify a posteriori for SMM1). Denoting $L_0(T)$ as the CO cooling rate coefficient (in erg s^{-1} cm^3) at temperature T, and X_{CO} and X_{H_2} as the CO and H_2 abundances relative to the total number density of H nuclei, $n_H = \rho_L/(1.4\, m_H)$, we have

$$\Lambda_{CO} = L_0(T_L)\, n(CO)\, n(H_2) = L_0(T_L)\, X_{CO}\, X_{H_2} \left(\frac{\rho_L}{1.4 m_H}\right)^2. \quad (37)$$

The ratio of turbulent heating to CO cooling is then independent of the mixing-layer density ρ_L. With a mean layer velocity $\overline{v_L} \simeq v_w/2$ (Couette flow), a typical value of $2\dot{M}_L$ within the Herschel beam of $2\Pi_L/R_b$ (see Equation (27)), and $2\Pi_L = \Pi_{BC}$, where Π_{BC} is the momentum in the warm CO broad component, this ratio can be expressed as

$$\frac{\Gamma_{visc}}{\Lambda_{CO}} = \left(\frac{c_L^2}{L_0(T_L) X_{CO} X_{H_2}}\right)\left(\frac{\pi R R_b v_w^2}{2\Pi_{BC}}\right)\left(\frac{\alpha}{\alpha_{max}}\right)(1.4\, m_H)^2$$
$$\simeq 0.4 \left(\frac{0.5}{X_{H_2}}\right)\left(\frac{c_L}{1\ km\ s^{-1}}\right)^2 \left(\frac{3\times 10^{-24}\ erg\ s^{-1}\ cm^3}{L_0(T_L)}\right)$$
$$\left(\frac{v_w}{30\ km\ s^{-1}}\right)^2 \left(\frac{R_b}{2400\ au}\right)$$
$$\times \left(\frac{R}{1000\ au}\right)\left(\frac{\alpha}{\alpha_{max}}\right)\left(\frac{8\times 10^{-2}\, M_\odot\ km\ s^{-1}}{\Pi_{obs}}\right). \quad (38)$$

It is remarkable that apart from X_{H_2}, there are no free parameters in this ratio, as all of the other factors are well constrained by observations of SMM1: the value of c_L is fixed by the relative intensities of the high-J CO lines, indicating $T_L \simeq 250$ K. The corresponding value of $L_0 \sim 3\times 10^{-24}$ erg s^{-1} cm^3 at 250 K is set by molecular collision rate calculations (Neufeld & Kaufman 1993). The value of v_w derives from our model fit to the CO(16−15) line profile in Figure 17. The cavity radius $R \simeq 1000$ au at $z = R_b = 2400$ au derives from our model fitting of the outflow shape in Figure 18. The value of $\alpha \simeq \alpha_{max}$ is required for our model to be consistent with the dust envelope infall rate in SMM1 (see Section 5.4). Finally, the product $\Pi_{BC}\, X_{CO}$ is equal to $\Pi_{obs} \times (5\times 10^{-5})$, where the value of $\Pi_{obs} = 8\times 10^{-2}\, M_\odot$ km s^{-1} is fixed by the observed CO line profile intensity and excitation temperature in SMM1 (see Equation (26)).

We conclude that if hydrogen is mostly in molecular form ($X_{H_2} \simeq 0.5$) and CO cooling is not far from the low-density regime, the ratio in Equation (38) is close to 1 for our mixing-layer model of SMM1 and thermal equilibrium can be maintained at the observed temperature ≃250 K of the broad CO $J = 16$–15 component.

The low-density CO cooling expression applies only until $L_0\, n(H_2) \simeq 0.5\, \mathcal{L}_{LTE}$, where $\mathcal{L}_{LTE}$ is the cooling rate per CO molecule in the high-density LTE regime. At 250 K, $\mathcal{L}_{LTE} \simeq 10^{-18}$ erg s^{-1} (Neufeld & Kaufman 1993), hence the validity extends to $n(H_2) \leqslant 1.7\times 10^5$ cm^{-3}. To estimate the density in the SMM1 mixing layer on the scale of the HIFI beam, we note that the shell pressure distribution on large scales is approximated by Equation (14). We infer the H nucleus density predicted in the mixing layer at $Z \simeq R_b$ for the SMM1 model parameters to be

$$n_H = \frac{P(R_b)}{1.4\, m_H c_L^2}, \simeq 1.4\times 10^5\ cm^{-3}\left(\frac{2400\ au}{R_b}\right)^{1.5}\left(\frac{\dot{M}_w}{6\times 10^{-6}\, M_\odot\ yr^{-1}}\right) \times \left(\frac{v_w}{30\ km\ s^{-1}}\right)\left(\frac{20{,}000\ au}{r_s}\right)^{0.5}\left(\frac{1\ km\ s^{-1}}{c_L}\right)^2. \quad (39)$$

If all hydrogen is in molecular form, we have $n(H_2) = 0.5 n_H \simeq 0.7\times 10^5$ cm^{-3} and the low-density regime of CO cooling assumed in Equation (38) is indeed justified for SMM1 on HIFI beam scales.

5.7. Summary and Discussion of the Model Fit to Protostar Serpens-Main SMM1

In summary, we have shown that our simple model of a turbulent mixing layer across a static wind/envelope interface is able to reproduce successfully all of the observed properties of the broad CO outflow component discovered by Herschel/HIFI in the Serpens-Main SMM1 protostar for a self-consistent and physically realistic set of parameters. The CO $J = 16$ – 15 line profile shape and velocity extent are reproduced for a typical wind speed $v_w \simeq 30$ km s^{-1} and a view angle of $\theta_{obs} = 30°$ to the disk plane (i.e., the median value expected for random inclinations). This wind speed is smaller than predicted for an X-wind from the innermost disk radius at ≃0.1 au ($v_w \simeq 150$ km s^{-1}; see, e.g., Shang et al. 1998) but remains compatible with a slow MHD disk wind launched from a few astronomical units in the disk (see, e.g., Tabone et al. 2020). Next, the observed outflow cavity size on 300–3000 au scales, when combined with the estimated dust temperature in the envelope, requires a ratio of wind mass flux to infall rate of 4%. With this imposed ratio, the observed CO-emitting momentum in the broad component (provided by wind entrainment) is consistent with the observed infall rate in the dusty envelope for a standard interstellar CO abundance and a turbulent entrainment coefficient $\alpha \simeq 0.03$ (consistent both with our assumption of a Couette flow in the mixing layer and with mixing-layer laboratory experiments). The corresponding wind mass flux then represents a fraction of ≃0.06–0.2 of the disk accretion rate onto SMM1 (as determined from its bolometric luminosity), consistent with current disk wind models. Finally, the observed temperature in the broad CO outflow component of SMM1 is consistent with a balance between turbulent heating and CO cooling in the mixing layer if H_2 is mostly in molecular form, which is very likely at such low temperatures. We also verify that the values of λ and Λ in our SMM1 model are consistent with the conditions for cavity breakout and the requirement of thin shells across the full range of disk radii expected in such a source, $r_d = 10$–300 au.

An obvious next step for this modeling work would be to compute self-consistently the time-dependent evolution of temperature and chemistry through the wind shock and along

the mixing layer, using for example the molecular MHD disk wind models of Panoglou et al. (2012) and Yvart et al. (2016) as initial conditions. Such a calculation would provide an important check on our model requirement of an interstellar CO abundance in the mixing layer of SMM1 to match independent constraints on the infall rate obtained from dust emission observations. It would also aid in the identification of the best tracer for the predicted narrow emission from the shocked wind layer (see black double-horned profile in Figure 17).

Furthermore, because our model assumes a steady wind-blown cavity, it provides a natural explanation not only for the broad Herschel-bright CO component but also for the narrow outflow cavity radii $\leqslant$3000 au observed at the Class 0 stage of 10^4–10^5 yr, despite observed CO velocities on the order of 10 km s^{-1}. In contrast, for wind-driven shell models with full mixing, quasi-radial outflow motions of the same amplitude lead to excessive cavity radii in only a few thousand years (see, e.g., Shang et al. 2006; López-Vázquez et al. 2019). Comparison over a larger sample of protostars with well-characterized broad components and outflow cavities will be necessary to verify that self-consistent models can be found, as in SMM1, and to investigate how the required wide-angle wind properties would need to vary with source properties.

6. Conclusions

In this paper, we have reconsidered the interaction of a wind expanding into a surrounding medium under the assumption of partial mixing across the boundary layer separating the shocked wind and envelope. Our solutions differ from conventional wind/envelope interaction models where instantaneous full mixing is assumed (e.g., Li & Shu 1996; Lee et al. 2000; López-Vázquez et al. 2019) in that we produce static, rather than expanding, shells. To maintain the stationary shape, we allow the shocked and deflected wind to flow upward at close to v_w along the interior of the cavity wall while the shocked and deflected envelope moves slowly downwards along the exterior of the cavity wall. A turbulent entrainment layer is thus able to form between these two deflected flows.

Specifically, we determine the shape of the stationary cavity formed when an isotropic wind interacts with an infalling and rotating (Ulrich 1976) envelope. The resulting model is then quantitatively compared with observations of the protostellar outflow from SMM1 in the Serpens Molecular Cloud.

The main results of our analysis are as follows:

1. The shape of the steady-state cavity (Section 2.3) is determined by two nondimensional parameters, λ, the ratio of the wind ram pressure to the fiducial infall ram pressure (Equation (8)), and Λ, the ratio of the wind ram pressure to the envelope thermal pressure at the edge of the disk (Equation (12)). We show that Λ sets the footpoint of the cavity at the disk plane (Figure 2) and that breakout solutions require $\lambda > 0.2$, with the cavity shapes becoming self-similar for $\lambda > 0.5$ (Figure 3). In the self-similar regime, the size scaling of the cavity is determined by r_s (Equation (10)).
2. Under the assumption of no mixing (Section 3.1), the shocked and deflected wind moves upward along the cavity at close to the velocity v_w, while the shocked and deflected envelope moves downward only slowly, except very near the base (Figure 7). Furthermore, away from the base, the associated downward momentum flux is much less than the upward momentum flux (Figure 8).
3. Under the assumption of partial mixing within a turbulent layer between the upward and downward shocked deflected layers (Section 3.2), the overall amount of material brought into the mixing layer, from both sides, is directly proportional to the mass-loss rate in the wind multiplied by the entrainment efficiency α and v_w/c_L (Figure 14). Furthermore, as previously shown by Cantó & Raga (1991), the mass entrainment from the upward, wind, side is roughly twice that of the downward, envelope, side (Figure 11), where the approximate proportionality is set by the assumption that across the mixing layer, the flow velocity profile is linear (i.e., a Couette flow).
4. The shape of the line profile produced by material flowing along the cavity wall strongly depends on which layer is responsible for the emission (Section 4.2). The upward, shocked wind layer moves fast, $v \sim v_w$, and has little curvature, resulting in a narrow profile peaked at the projected wind velocity. Alternatively, due to the Couette-type flow, emission from the mixing layer is broad and peaks at rest velocity (Figures 16 and 17).
5. We find an excellent correspondence between the broad component of the CO $J = 16 - 15$ line profile observed by Herschel toward the protostar Serpens-Main SMM1, and a mixing-layer model with $v_w =$ 25–30 km s^{-1}, a viewing angle 30° from the disk plane, and an emissivity proportional to density (Section 5). Furthermore, taking $\alpha \simeq 0.03$, a value that matches very well with experimental measurements of supersonic mixing, and assuming a standard CO abundance and a reasonable ratio of wind to infall rate of 4%, we find excellent quantitative agreement between the observed momentum in the CO broad component, the observed infall rate of SMM1, and the observed outflow cavity size (Section 5.4).
6. We compute the turbulent heating, expansion cooling, and radiative CO cooling within the mixing layer and show that their ratio is appropriate to keep the gas warm at the observed temperature $T_L \simeq 250$ K in SMM1 (Section 5.6).
7. Finally, our model provides a natural explanation for the narrow outflow cavity radii observed at the Class 0 stage of 10^4–10^5 yr (Section 5.7). Unlike wind-driven shell models with full mixing, in which radial motions quickly lead to large cavity sizes, our partial mixing solutions with a mixing layer separating the shocked wind and envelope produce a time-independent, steady cavity where observed velocities are parallel to the cavity walls and thus do not lead to excessive expansion.

To summarize, we provide a model for the interaction between a wind and a surrounding envelope that potentially can be applied widely, from protostellar outflows to galactic scales. The model produces steady-state cavities and broad-line profiles peaked at the rest velocity, and constrains the turbulent entrainment efficiency. It therefore provides a new framework in which to interpret the observations of warm wind-driven outflows, and in particular to reconcile modest outflow cavity widths with the large observed flow velocities. While the model successfully reproduces a number of observational constraints for a single protostellar outflow, Serpens-Main SMM1, an obvious next step is to apply this analysis to a larger sample of

protostellar sources in order to test its success; this will be done in a forthcoming publication.

We thank the anonymous referee for comments that improved this paper. D.J. is supported by the National Research Council of Canada and by a Natural Sciences and Engineering Research Council of Canada (NSERC) Discovery Grant. The work of S.C. is supported by the Programme National Physique et Chimie du Milieu Interstellaire (PCMI) of CNRS/INSU with INC/INP and cofunded by CNES, and by the Conseil Scientifique of Observatoire de Paris. The research of L.E.K. is supported by a research grant (19127) from VILLUM FONDEN. Research at the Centre for Star and Planet Formation is funded by the Danish National Research Foundation.

D.J. would like to thank the Observatoire de Paris, the Observatoire de Grenoble, and the European Southern Observatory in Garching, Germany for hosting him during visits at which many detailed discussions for this paper took place. D.J. and S.C. also thank the Herschel WISH team, especially Ewine van Dishoeck, for strongly encouraging this research project. Our investigation into steady wind-blown cavities began a full decade ago following an off-the-cuff remark during a WISH team breakout session at the "5th Zermatt ISM Symposium." Within the WISH consortia, this project has been colloquially named the "Doug and Sylvie Show."

Appendix A
The Boundary Condition of the Interface at the Disk Plane

We determine the boundary condition of the interface at the disk plane by requiring pressure balance between the stellar wind and envelope sides. This directly leads to a one-to-one relation between R_0 (the distance of the wind/envelope interface from the central star at the disk plane) and β_0 (the angle of incidence at the base). Formally,

$$\sin^2\beta_0 = \Lambda^{-1}(R_0/r_{\rm d})^{3/2}/(1 - R_0/r_{\rm d}), \tag{A1}$$

which depends on Λ. In Figure A1, we show β_0 as a function of R_0 for $\Lambda = 25$ (magenta line), 50 (blue line), 100 (red line), and 200 (solid black line). For the purpose of reference, we also show in the same figure the local angle of incidence of the infalling envelope gas at the midplane as a function of R_0 (dotted black line).

It can be seen that for a given Λ, the allowed angle of incidence of the interface increases monotonically with R_0 and reaches $\pi/2$ near $r_{\rm d}$ for all Λ values that we have considered in this paper ($\beta_0 = \pi/2$ indicates that the interface is perpendicular to the disk plane). In the inner region, we find that the incidence angle of the envelope material at the disk plane

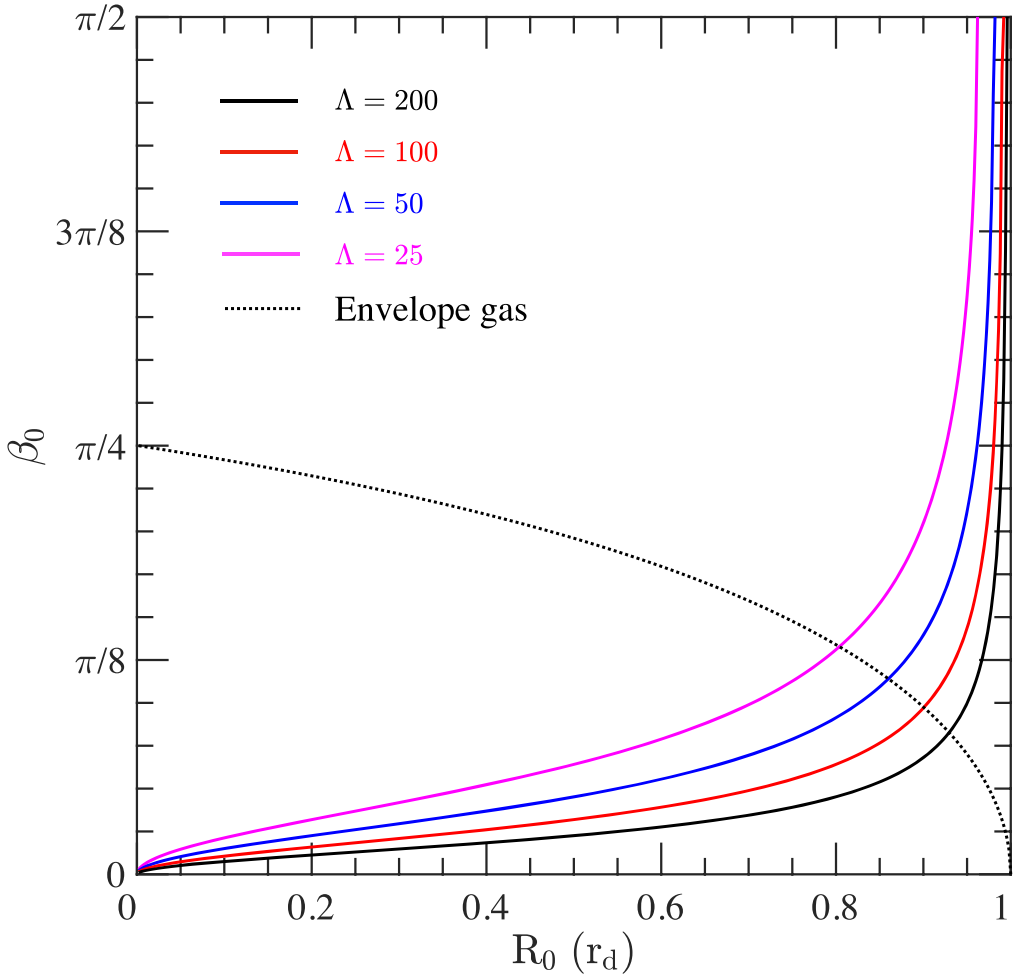

Figure A1. The allowed angle of incidence of the wind–envelope interface at the disk plane as a function of R_0, for models with different Λ values. The dotted black line indicates the angle of incidence of the infalling material at R_0.

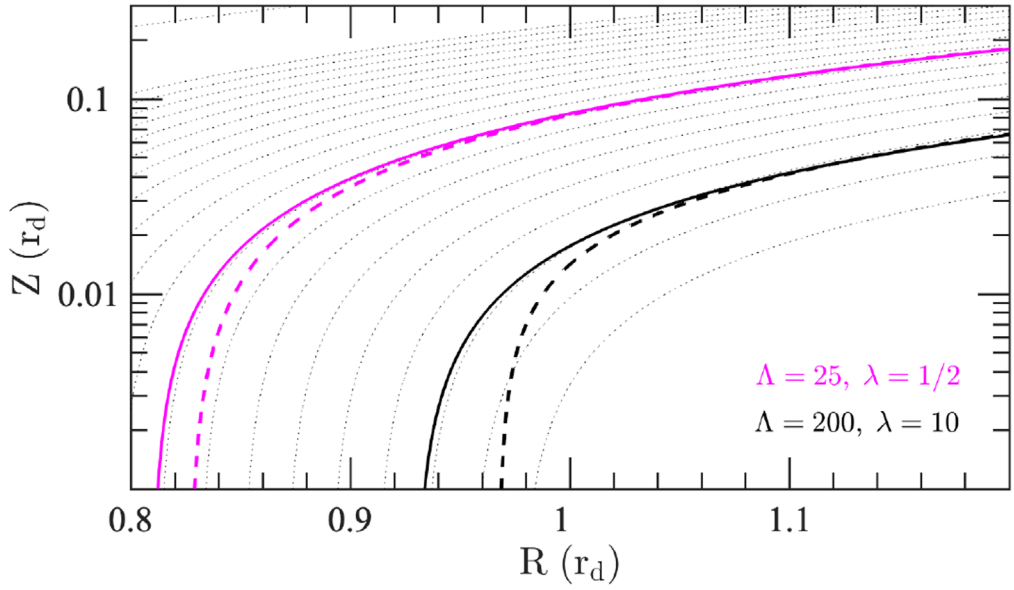

Figure A2. Cavity shapes near the base for an isotropic wind colliding with an Ulrich (1976) infalling envelope for different Λ values. The magenta and black lines correspond to the model of ($\Lambda = 25$, $\lambda = 1/2$) and ($\Lambda = 200$, $\lambda = 10$), respectively. For each model, the solid curve represents the "fiducial" solution where the wind/envelope interface at the footpoint lies parallel to the local streamline of the material of the infalling envelope at the disk plane, whereas the dashed line represents a different solution where the base of the interface is located at a larger R_0. For a given Λ, the solutions of different base positions converge at a small distance from the disk plane (a few $0.01 r_d$). The thin dotted lines in the background indicate the streamlines of the material within the infalling envelope.

becomes larger than the allowed β_0 of the wind/envelope interface. This corresponds to an unphysical solution where the envelope gas pushes the interface from the same side as the stellar wind. It is therefore a requirement that R_0 is sufficiently large so that a stable wind/envelope interface that is balanced by the pressure of the stellar wind and infalling envelope from either side is possible.

For the fiducial models presented in the paper, the wind/envelope interfaces at the footpoint are parallel to the local streamline of the material of the infalling envelope at the disk plane (corresponding to the intersecting point between the dashed line and each colored solid line in Figure A1). For a given Λ, when the interface footpoint is placed at a somewhat larger R, the cavity quickly converges to the fiducial case within a small distance from the base, as is shown in Figure A2. The footpoint, however, cannot become arbitrarily close to r_d without the infalling material crushing the wind and preventing a breakout solution, dependent on the value of λ. Thus, the footpoint location is highly constrained, with larger λ values allowing a broader range of solutions at the base, all converging to self-similar solutions at altitude.

Appendix B
Equations for the Growth of the Mixing Layer

Several typographical errors were present in the general equations from Raga et al. (1995) describing the growth of the mixing layer between two axisymmetric moving fluids of speed v_1 and $v_2 < v_1$: in their Equation (13), the term hP' should have been $-hP'$, while in their Equation (16), the factor r_c next to $(h_1 + h_2)P'$ should not be present. Below, we reproduce their Equations (15) and (16) where the latter typo has been corrected, and we use the subscript "L" to denote quantities in the mixing layer, instead of the lower case letter "l," which was difficult to differentiate from the digit "1" in Raga et al. (1995). Furthermore, for consistency with the notation in the main paper, here we refer to the velocity within the mixing layer as v_L whereas in Raga et al. (1995) it is just v. All other notations are kept the same. Because we assume an isothermal mixing layer with uniform sound speed c_L, we do not have to integrate their energy equation. Thus the system reduces to solving the following set of coupled equations for $h_1(x)$ and $h_2(x)$, which are the respective widths by which the mixing layer encroaches into each fluid:

$$(\rho_1 v_1 - \rho_L \overline{v_L})\frac{dh_1}{dx} + (\rho_2 v_2 - \rho_L \overline{v_L})\frac{dh_2}{dx} - (h_1 + h_2)\overline{v_L}\frac{d\rho_L}{dx} = \rho_L (h_1 + h_2)\frac{(\overline{v_L} r_c)'}{r_c} - \alpha \rho_L c_L \tag{B1}$$

and

$$(\rho_1 v_1^2 - \rho_L \overline{v_L^2})\frac{dh_1}{dx} + (\rho_2 v_2^2 - \rho_L \overline{v_L^2})\frac{dh_2}{dx} - (h_1 + h_2) \times \overline{v_L^2}\frac{d\rho_L}{dx} = \rho_L (h_1 + h_2)\frac{(\overline{v_L^2} r_c)'}{r_c} - \alpha \rho_L c_L v_2 + (h_1 + h_2)P'. \tag{B2}$$

In these equations, the subscript "1" denotes quantities pertaining to the fast fluid (in our case, the deflected wind), the subscript "2" pertains to the slow fluid (in our case, the deflected envelope), x is the distance along the flow, r_c and P are the cylindrical radius and the pressure at the current point, respectively, primes denote derivatives versus x, and the mean velocities in the mixing layer for a linear Couette flow are given by

$$\overline{v_L} = \frac{v_1 + v_2}{2} \tag{B3}$$

and

$$\overline{v_{\rm L}^2} = \frac{v_1^3 - v_2^3}{3(v_1 - v_2)}. \quad \text{(B4)}$$

The mass densities in the three layers are determined through transverse pressure equilibrium as

$$\rho_1 c_1^2 = \rho_2 c_2^2 = \rho_{\rm L} c_{\rm L}^2 = P, \quad \text{(B5)}$$

where we assume here for simplicity that the sound speeds c_1, c_2, and $c_{\rm L}$ do not vary with position.

An added complication for our paper is that our two fluids do not flow in the same direction. Fortunately, we always have $v_2 < v_{\rm d} \ll v_1 \simeq v_{\rm w}$. We thus assume $v_2 = 0$ when integrating these equations upward along x, i.e., that mass entrainment into the mixing layer from the slow envelope side is largely dominated by the turbulent entrainment term.

Appendix C
Viscous Dissipation in the Mixing Layer

We consider the simplified case, relevant to the present paper, of an isothermal, supersonic mixing layer of width h between two fluids with $v_2 \simeq 0$ and $v_1 \gg v_2$, and with a linear velocity gradient across the flow direction (Couette profile) $dv(y)/dy \simeq (v_1/h)$ where v_1 changes weakly with position x along the flow.

We calculate $\Gamma_{\rm visc}$, the excess kinetic energy that needs to be locally dissipated by viscous turbulence per unit time and volume within the layer to maintain its internal linear Couette profile as follows. The flux of kinetic energy flowing along the mixing layer is given by

$$\begin{aligned}\dot{E}(x) &= 2\pi R \int_0^h \rho_{\rm L}\left[\frac{v(y)^3}{2}\right]dy,\\ &= 2\pi R \rho_{\rm L} h \frac{v_1}{2}\left[\frac{v_1^2}{4}\right],\\ &= \dot{M}_{\rm L}(x)\left[\frac{v_1^2}{4}\right]. \end{aligned} \quad \text{(C1)}$$

Note that in converting to units of mass flow in the layer, $\dot{M}_{\rm L}$, we make use of the fact that the mean flow velocity in the layer is $\overline{v_{\rm L}} = v_1/2$ (Couette profile with $v_2 \simeq 0$).

We next consider a "slice" of the mixing layer of thickness Δx and denote $\dot{E}_{\rm in}$ and $\dot{E}_{\rm out}$, the kinetic energy flux flowing through the layer at positions x and $x + \Delta x$, respectively. Because v_1 is considered constant with position, the change in kinetic energy flux (Equation (C1)) between x and $x + \Delta x$ is caused only by the increase in mass flux through the layer, $\Delta\dot{M}_{\rm L}$, via sideways entrainment. Recalling that to maintain a Couette flow with $v_2 \simeq 0$ the entrainment rate from the wind side must be twice that from the ambient side (see Section 3.2), we then have

$$\dot{E}_{\rm out} - \dot{E}_{\rm in} = \Delta\dot{M}_{\rm L}\left[\frac{v_1^2}{4}\right] = 3\rho_2 v_{\rm ent}(2\pi R\Delta x)\left[\frac{v_1^2}{4}\right]. \quad \text{(C2)}$$

At the same time, the kinetic energy flux $\dot{E}_{\rm ent}$ injected into the slice through its lateral surfaces by entrainment of fresh wind material at v_1 is given by

$$\dot{E}_{\rm ent} = 2\rho_2 v_{\rm ent}(2\pi R\Delta x)\left[\frac{v_1^2}{2}\right]. \quad \text{(C3)}$$

The excess injected kinetic energy that needs to be dissipated by turbulent viscosity per unit time within the slice volume to maintain the Couette flow is

$$\dot{E}_{\rm visc} = \dot{E}_{\rm ent} + \dot{E}_{\rm in} - \dot{E}_{\rm out} \equiv \Gamma_{\rm visc}(2\pi R\Delta x)h. \quad \text{(C4)}$$

Combining Equations (C2)–(C4), we obtain

$$\begin{aligned}\Gamma_{\rm visc} &= \frac{\rho_2 v_{\rm ent}}{h}\left[v_1^2 - \frac{3v_1^2}{4}\right]\\ &= \frac{\rho_2 v_{\rm ent}}{h}\left[\frac{v_1^2}{4}\right] = \frac{\alpha}{4}\rho_{\rm L} c_{\rm L} h\left(\frac{v_1}{h}\right)^2, \end{aligned} \quad \text{(C5)}$$

where we make use of our prescription for $v_{\rm ent} \equiv \alpha\, c_2^2/c_{\rm L}$ and recognize the lateral pressure equilibrium across the shell, $\rho_2 c_2^2 = \rho_{\rm L} c_{\rm L}^2$. Comparing Equation (C5) with the standard expression for viscous dissipation, $\Gamma_{\rm visc} = \mu(dv(y)/dy)^2$, we obtain an "effective" turbulent viscosity in the mixing layer

$$\mu = \frac{\alpha}{4}\rho_{\rm L} c_{\rm L} h. \quad \text{(C6)}$$

Note that we recover the same turbulent viscosity prescription as in Equation (5) of the work of Binette et al. (1999; with their parameter α being one-fourth of our α). For the typical $\alpha = 0.03$ favored by mixing-layer experiments (Cantó & Raga 1991), the numerical coefficient in Equation (C6) would be $\simeq$0.007, as adopted by Binette et al. (1999) for their calculations.

ORCID iDs

Lichen Liang https://orcid.org/0000-0001-9422-0095
Doug Johnstone https://orcid.org/0000-0002-6773-459X
Sylvie Cabrit https://orcid.org/0000-0002-1593-3693
Lars E. Kristensen https://orcid.org/0000-0003-1159-3721

References

Aalto, S., Costagliola, F., Muller, S., et al. 2016, A&A, 590, 73
Aalto, S., Muller, S., Costagliola, F., et al. 2017, A&A, 608, 22
Binette, L., Cabrit, S., Raga, A., & Cantó, J. 1999, A&A, 346, 260
Bondi, H. 1952, MNRAS, 112, 195
Brral, J. F., & Cantó, J. 1981, RMxAA, 5, 101
Cabrit, S., Ferreira, J., & Raga, A. C. 1999, A&A, 343, L61
Cantó, J., & Raga, A. C. 1991, ApJ, 372, 646
Delamarter, G., Frank, A., & Hartmann, L. 2000, ApJ, 530, 923
Downes, T. P., & Cabirt, S. 2003, A&A, 403, 135
Enoch, M. L., Corder, S., Dunham, M. M., & Duchêne, G. 2009, ApJ, 707, 103
Enoch, M. L., Evans, N. J., Sargent, A. I., et al. 2008, ApJ, 684, 1240
Frank, A., Ray, T. P., Cabrit, S., et al. 2014, in Protostars and Planets VI, ed. H. Beuther et al. (Tucson, AZ: Univ. Arizona Press), 451
Goicoechea, J. R., Cernicharo, J., Karska, A., et al. 2012, A&A, 548, 77
Gueth, F., Guilloteau, S., & Bachiller, R. 1998, A&A, 333, 287
Herczeg, G. J., Kuhn, M. A., Zhou, X., et al. 2019, ApJ, 878, 111
Hosokawa, T., & Homukai, K. 2009, ApJ, 691, 823
Hull, C. L. H., Girat, J. M., Kristensen, L. E., et al. 2016, ApJL, 823, L27
Hull, C. L. H., Girat, J. M., Tchoniec, K., et al. 2017, ApJ, 847, 92
Kristensen, L. E., & Dunham, M. M. 2018, A&A, 618, 158
Kristensen, L. E., van Dishoeck, E. F., Benz, A. O., et al. 2013, A&A, 557, 23
Kristensen, L. E., van Dishoeck, E. F., Bergin, E. A., et al. 2012, A&A, 542, A8

Kristensen, L. E., van Dishoeck, E. F., Mottram, J. C., et al. 2017, A&A, 605, 93
Le Gouellec, V. J. M., Hull, C. L. H., Maury, A. J., et al. 2019, ApJ, 885, 106
Lee, C.-F., Hirano, N., Zhang, Q., Shang, H., & Ho, P. T. P. 2015, ApJ, 805, 186
Lee, C.-F., Mundy, L. G., Reipurth, B., Osriker, E. C., & Stone, J. M. 2000, ApJ, 542, 925
Li, Z.-Y., & Shu, F. H. 1996, ApJ, 486, 261
López-Vázquez, J. A., Cantó, J., & Lizano, S. 2019, ApJ, 879, 42
Margulis, M., & Snell, R. L. 1989, ApJ, 343, 779
Matsuyama, I., Johnstone, D., & Hollenbach, D. 2009, ApJ, 700, 10
Maury, A., André, Ph., Testi, L., et al. 2019, A&A, 621, A76
Mendoza, S., Cantó, J., & Raga, A. C. 2004, RMxAA, 40, 147
Mottram, J. C., Kristensen, L. E., van Dishoeck, E. F., et al. 2014, A&A, 572, 21
Mottram, J. C., van Dishoeck, E. F., Kristensen, L. E., et al. 2017, A&A, 600, 99
Neufeld, D. A., & Kaufman, M. J. 1993, ApJ, 418, 263
Ostricker, E. C., Lee, C.-F., Stone, J. M., & Mundy, L. G. 2001, ApJ, 557, 443
Panoglou, D., Cabrit, S., Forêts, Pineau Des., et al. 2012, A&A, 538, 2
Pilbratt, G. L., Riedinger, J. R., Passvogel, T., et al. 2010, A&A, 518, L1
Raga, A., & Cabrit, S. 1993, A&A, 278, 267
Raga, A. C., Cabrit, S., & Cantó 1995, MNRAS, 273, 442
Shang, H., Allen, A., Li, Z.-Y., et al. 2006, ApJ, 649, 845
Shang, H., Glassgold, A. E., Shu, F. H., & Lizano, S. 2002, ApJ, 564, 853
Shang, H., Shu, F. H., & Glassgold, A. E. 1998, ApJL, 493, L91
Smith, M. D. 1986, MNRAS, 223, 57
Tabone, B., Cabrit, S., Pineau des Forets, G., et al. 2020, A&A, in press (arXiv:2004.08804)
Tobin, J. J., Hartmann, L., Bergin, E., et al. 2012, ApJ, 748, 16
Ulrich, R. K. 1976, ApJ, 210, 377
van Dishoeck, E. F., Kristensen, L. E., Benz, A. O., et al. 2011, PASP, 123, 138
Wilkin, F. P., & Stahler, S. W. 2003, ApJ, 590, 917
Yildiz, U. A., Kristensen, L. E., van Dishoeck, E. F., et al. 2013, A&A, 556, 89
Yvart, W., Cabrit, S., Pineau des Fôrets, G., & Ferreira, J. 2016, A&A, 585, 74